Stony Brook University

Tidal and Residual Circulation in Long Island Sound

A Dissertation Presented

by

Yan Hao

to

The Graduate School

in Partial fulfillment of the

Requirements

for the Degree of

Doctor of Philosophy

in

Marine and Atmospheric Science

Stony Brook University

May 2008

Stony Brook University

The Graduate School

Yan Hao

We, the dissertation committee for the above candidate for the

Doctor of Philosophy degree, hereby recommend

acceptance of this dissertation.

Robert E. Wilson - Dissertation Advisor
Associate Professor, School of Marine and Atmospheric Sciences

Dong-Ping Wang - Chairperson of Defense
Professor, School of Marine and Atmospheric Sciences

Charles N. Flagg
Professor, School of Marine and Atmospheric Sciences

Edmund K.M. Chang
Professor, School of Marine and Atmospheric Sciences

Clinton D. Winant
Professor, Physical Oceanography
SCRIPPS Institution of Oceanography, University of California, San Diego

This dissertation is accepted by the Graduate School

Lawrence Martin
Dean of the Graduate School

Abstract of the Dissertation

Tidal and Residual Circulation in Long Island Sound

by

Yan Hao

Doctor of Philosophy

in

Marine and Atmospheric Science

Stony Brook University

2008

A three-dimensional numerical hydrodynamic model for Long Island Sound is applied to examine the spatial structure of the tidal and residual circulation in the basin. Momentum diagnostics are used to analyze the dynamics controlling the longitudinal and lateral circulation. At tidal periods, the longitudinal momentum balance involves local acceleration, barotropic pressure gradient, and stress divergence; the lateral momentum balance involves local acceleration, barotropic pressure gradient, and Coriolis acceleration, with some contribution from the baroclinic pressure gradient at depth. Tidal period lateral circulation is driven primarily by the imbalance between barotropic pressure gradient and Coriolis acceleration. The residual longitudinal momentum balance involves primarily longitudinal advection and the total longitudinal pressure gradient. Results indicated that residual longitudinal advection arises from the interaction of tidal period lateral motion and lateral gradients in longitudinal tidal currents. They indicate further that residual longitudinal advection and longitudinal baroclinic pressure gradient represent driving forces of the same order throughout much of the basin. The residual lateral momentum balance is essentially geostrophic. Results are consistent with recent theoretical models for tidal and residual circulation in elongated rotating basins. Features of the simulated tidal period and residual current structure compare favorably with those features derived from available ADCP current observations in the central Long Island Sound.

Table of Contents

List of Figures

Chapter 1.

Chapter 2.

Chapter 3.

Chapter 4.

Chapter 5.

List of Tables

Acknowledgements

I would like to thank my advisor, Dr. Robert E. Wilson, for his great patience and guidance. I have learned so many things from him over the years. I can not make all these achievements without him.

I would like to thank my committee: Dr. Dong-Ping Wang, Dr. Charles N. Flagg, Dr. Edmund K.M. Chang and Dr. Clinton D. Winant for their comments and suggestions, which improved this work tremendously.

I would like to thank New York Sea Grant and US EPA Long Island Sound Study (under Grant Numbers LI972862040 and LI972862050) for their financial supports.

I would like to thank my friends for loving me and helping me.

I would like to thank my husband Jianhua, my son Augie, my father Yunxian and my MOTHER XIUMEI for all the love and supports they gave me.

Chapter 1

Introduction and Objectives

There is increasing understanding of three-dimensional structure of tidal currents and residual currents in estuaries developed from both observations and three-dimensional numerical simulations, and of the importance of this structure to transport and dispersion of dissolved and suspended materials (Geyer and Chant, 2008). These observations and simulations are also leading to an understanding of the dynamics responsible for the observed structure in tidal and residual currents. There have been very few analytical studies related to the three-dimensional structure of tidal and residual currents in estuaries. Notable exceptions include analyses by Winant (2007) and Winant (2008). There is, in addition, a recent relevant two-dimensional analytical study by Huijts et al (2008).

Observations and simulations to date have focused on narrow estuaries such as the Hudson River or narrow tributary estuaries to the Chesapeake Bay. In this study we present a description of the three-dimensional structure of both tidal and residual currents in Long Island Sound as representative of wide estuary.

1.1 Recent studies of the three-dimensional structure of tidal currents

Recent observations, in addition to providing a description of the vertical and lateral structure of longitudinal tidal currents, have revealed the existence of significant lateral tidal period motion, even in narrow estuaries. Observations by Valle-Levinson et al. (2000) in the James River estuary revealed the existence of lateral tidal flow with

amplitude of 20% of the axial flow. Geyer et al. (2000) found a vertically sheared lateral tidal circulation in the lower Hudson River estuary with maximum amplitude of approximately 10%-15% of the axial flow. The effects of channel curvature on tidal period secondary circulation have been described in the Hudson by Chant and Wilson (1997) and Chant (2002), and by Lacey and Monismith (2001) in an estuarine channel in northern San Francisco Bay.

Informative numerical models of the three-dimensional structure of tidal flow in estuaries are those by Lerczak and Geyer (2004), Cheng (2007), Cheng et al. (2008), and Chen and Sanford (2008). The model by Lerczak and Geyer (2004) provided a description of tidal period lateral motion for a straight channel in which lateral circulation was driven primarily by the lateral baroclinic pressure gradient produced by differential advection of the longitudinal salinity gradient. Simulations by Chen and Sanford (2008) emphasized the influence of a lateral baroclinic pressure gradient produced by boundary mixing on tidal period lateral flow. Simulations by Cheng (2007) and Cheng et al. (2008) for the Passaic estuary provided evidence for the combined effects of Coriolis forcing, differential advection and boundary mixing on lateral tidal currents.

The analytical model developed by Winant (2007) provided a description of the three-dimensional structure of barotropic tidal currents in an elongated, rotating co-oscillating basin. For this barotropic model, lateral motion is driven only by Coriolis forcing associated with the imbalance between the cross-channel sea level gradient and the Coriolis acceleration associated with the vertically sheared axial flow. Winant (2007) explored the sensitivity of the structure of longitudinal and lateral flow to the aspect ratio $\alpha=B/L$, where B is the basin width and L is the channel length, and friction as

represented by the parameter $\delta=(2K/\omega H^2)^{1/2}$, which is the ratio of the amplitude of the periodic boundary layer thickness to water column depth, where K is the vertical eddy viscosity and ω is the angular tidal frequency. Details of model scaling are discussed in Chapter 3.

1.2 Recent studies of the three-dimensional structure of residual currents

Systematic studies of the three-dimensional structure are limited. Three-dimensional numerical simulations by Lerczak and Geyer (2004) showed that for the residual longitudinal momentum balance, tidally averaged advective accelerations could have comparable magnitude to the longitudinal baroclinic pressure gradient, as so affect the structure of residual axial currents. The analytical model developed by Winant (2008) provided a description of the three-dimensional structure of tidal residual currents in an elongated, rotating co-oscillating basin. In this model, residual currents are driven by residual advective terms associated with the barotropic tidal motion. Advection is produced by the lateral advection of axial momentum associated with the Coriolis forced lateral motion. Advection tends to drive a laterally and vertically sheared residual motion with an inflow on the right side of the basin and an outflow on the left side of the basin. Winant (2008) explored the sensitivity of the structure of residual longitudinal and lateral flow to the aspect ratio α and friction parameter δ. Details of model scaling are discussed in Chapter 4.

A two-dimensional analytical study by Huijts et al. (2008) diagnosed the lateral structure of longitudinal and lateral residual flows in an estuary in response of both advection and a longitudinal density gradient in the presence of rotation. In their

analysis, advection was produced by the same mechanism as that represented in Winant (2008), that is, through lateral advection of axial momentum associated with the Coriolis induced lateral motion. Huijts et al. (2008) presented a description of the characteristic lateral structure of longitudinal and lateral residual flows for advective and density forcing. For advective forcing, the structure of advective accelerations and the residual currents were consistent with results presented by Winant (2008) for intermediated values of δ. For density forcing, the structure of residual longitudinal currents was consistent with that proposed by Kasai et al. (2000), that is, inflow concentrated over the deep channel and outflow concentrated of the channel flanks. Residual current structure for combined advective and density forcing would be expected to be laterally asymmetric. Huijts et al. (2008) also obtained velocity scales for individual flow components. For forcing associated with and imposed by longitudinal density gradient and by tidal advection, the longitudinal residual velocity scales as: $\frac{H_{\max}^3}{48K}\frac{g\partial\rho}{\rho_0\partial x}$ and $\frac{f}{\omega}\frac{Q^2}{2B^2KL_y}$ respectively, where H_{max} is the maximum channel depth, K is the vertical eddy viscosity, ω is the angular tidal frequency, Q is the amplitude of the semi-diurnal tidal discharge, B is the channel width, and $L_y=L^2/B$ is a topographic scale where L is a lateral bathymetric steepness parameter associated with the Gaussian channel bathymetry given by $H=H_{max}\exp(-(y-B/2)^2/L^2$. The velocity scale associated with longitudinal density gradient forcing was first derived by Officer (1976). The second velocity scale associated with forcing by tidal advection produced by tidal period lateral motion driven by Coriolis forcing.

1.3 Recent studies of Long Island Sound

Long Island Sound (LIS) (Fig. 1.1) is an estuary located between Long Island, NY and Connecticut. It communicates with the Atlantic Ocean through Block Island Sound at its eastern end, and with the lower Hudson Estuary through the East River at its western end. LIS is a glacial terminal moraine with unique topographic features (Fig. 1.2). The basin is approximately 150 km long and 34 km wide at its widest point. Bathymetry is characterized by an asymmetrical V-shaped channel cross-section with maximum channel depths in excess of 60 m. Two broad sills run obliquely across the basin.

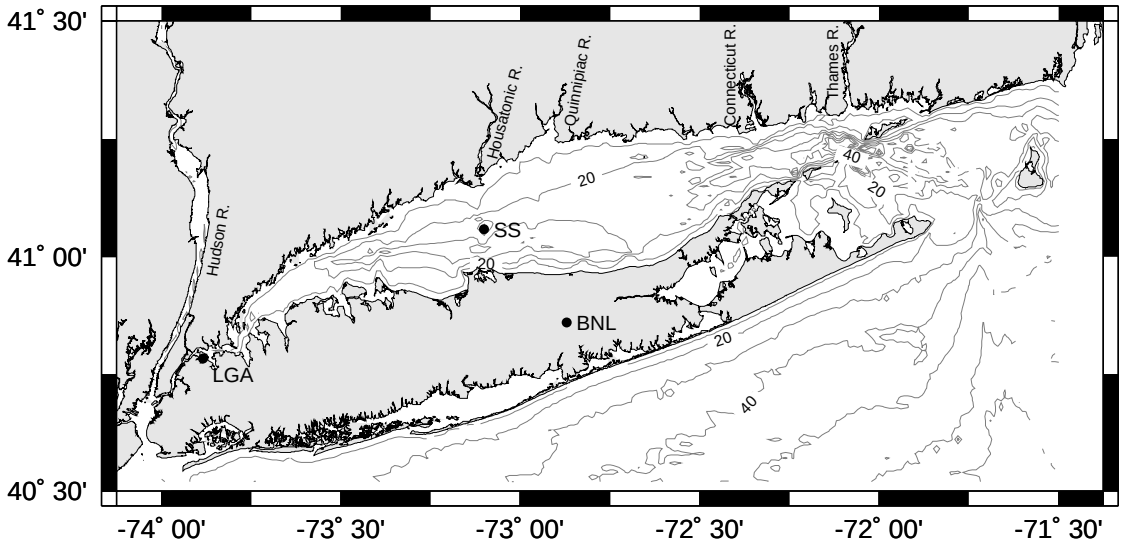

Figure 1.1 Map of Long Island Sound

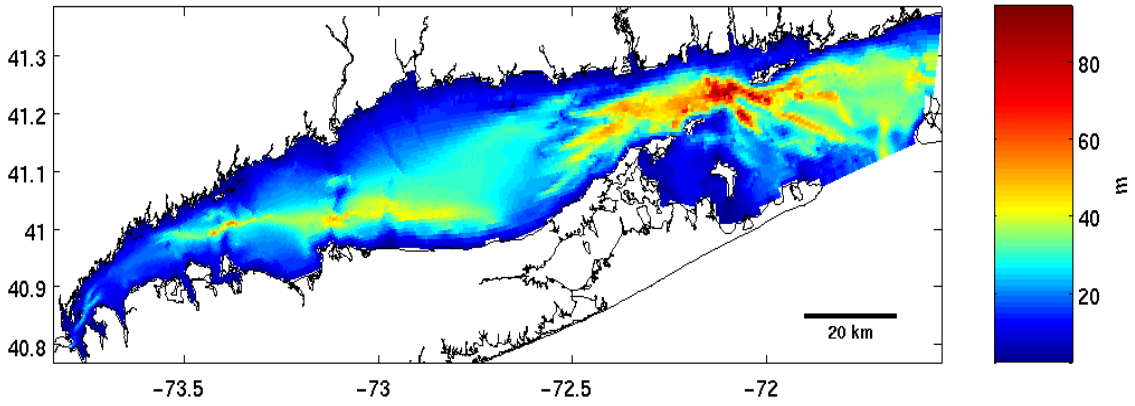

Figure 1.2. Long Island Sound bathymetry

Tides in LIS co-oscillate with those in Block Island Sound and are nearly resonant at the semi-diurnal period. They exhibit standing wave characteristics in the central and western basin, and nearly progressive wave characteristics in the eastern basin. Amplitudes of the M_2, S_2, N_2 constituents at New London, CT at the eastern end of the basin are 0.37 m, 0.067 m and 0.087 m, respectively. This leads to strong fortnightly and monthly modulation.

The major sources of direct fresh water input into LIS are rivers along the CT coast. The Connecticut River with a mean annual discharge of 560 m^3/s contributes 72% of the total freshwater input to the basin. The buoyancy flux through East River maintains the longitudinal salinity and density gradients within the basin which drives the gravitational circulation.

The most contemporary description of basin hydrography is provided by Crowley (2005) who studied the seasonal evolution of thermohaline circulation in LIS and the associated heat and salt budgets. Fig. 1.3 shows longitudinal sections of temperature, salinity and σ_t along the channel axis averaged over a summer period extending from

June 29, 1988 through August 25, 1988. These sections are from three-dimensional numerical simulations which involved the assimilation of extensive hydrographic observations during 1988. They show a surface intensified stratification with a surface to bottom density difference of approximately 3 kg/m^3. They also indicate a longitudinal density difference over the length of the basin of approximately 5 kg/m^3. Fig. 1.4 shows the lateral structure of temperature, salinity and σ_t along a lateral section in the central basin with mean longitude -72.93^o for the same summer period. These sections point to a bottom mixed layer which is especially well developed on the northern flank of the channel, and which contributes to lateral density gradients within the bottom mixed layer. The sections also show a core of cold saline water within the channel which is moving towards the west.

There has not been any systematic description of tidal or residual currents in LIS. Bogden and O'Donnell (1998) applied a simple linear shallow-water model forced by tidal boundary conditions to predict tide height and depth averaged tidal currents in central LIS. They attempted to subtract predicted tidal currents from observations obtained from a limited area ADCP survey in central LIS, but found that the linear shallow-water dynamics on which their model was based were not accurate enough for this purpose.

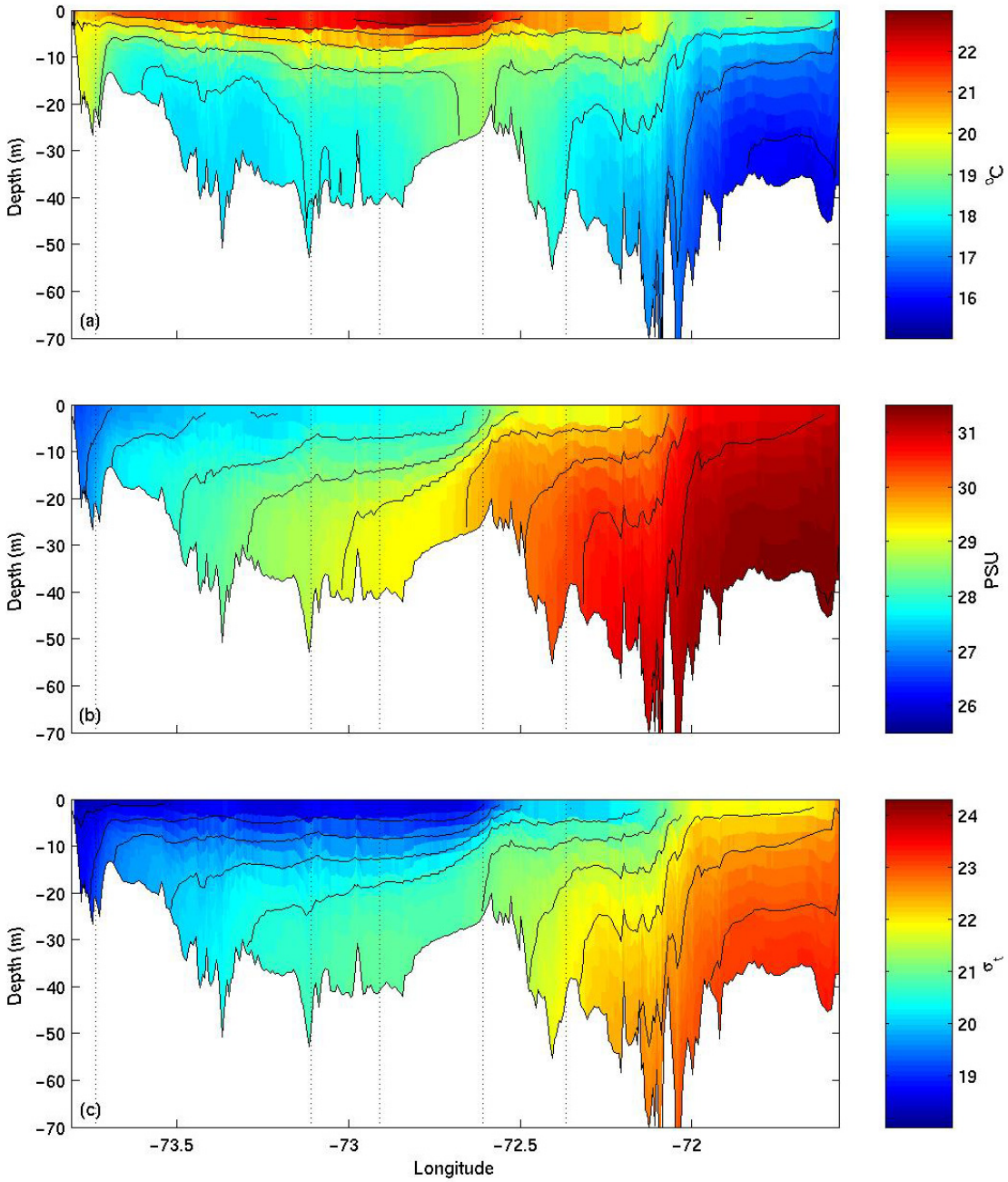

Figure 1.3. Sections of seasonally averaged values of (a) temperature, (b) salinity and (c) σ_t along the thalweg of Long Island Sound for summer. (Crowley, 2005)

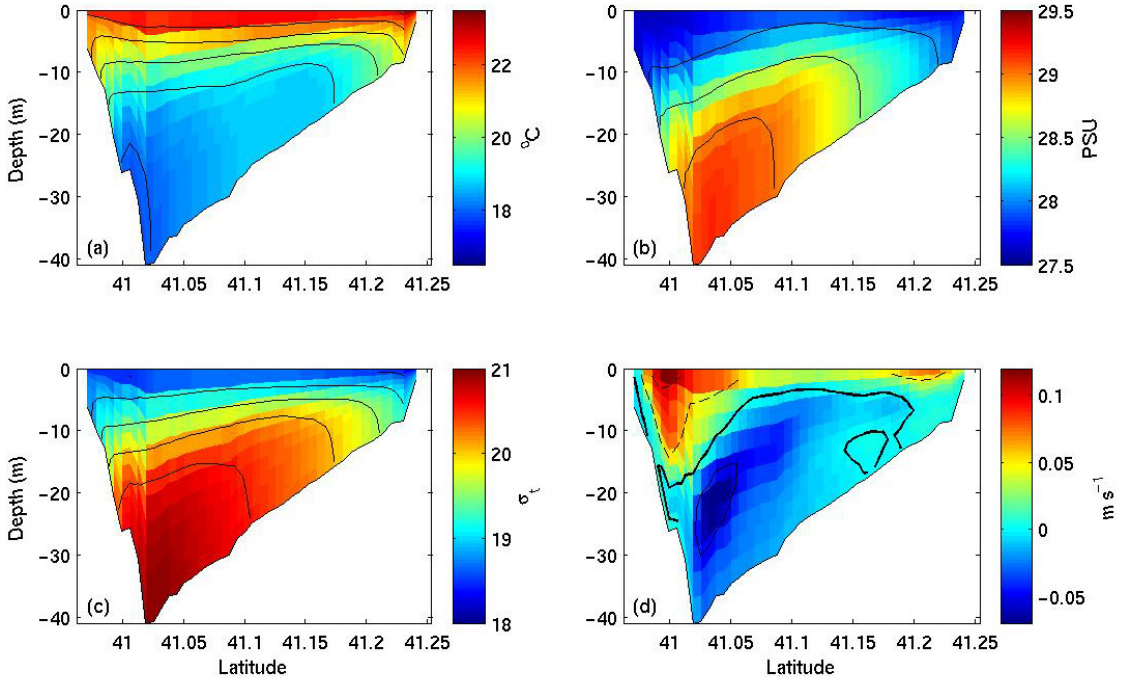

Figure 1.4. Sections of seasonally averaged values of (a) temperature, (b) salinity, (c) σ_t and (d) u-component of current velocity at column 144 for summer. (The heavy black line in (d) indicates velocity = 0.) (Crowley, 2005)

Vieira (2000) analyzed the moored currents data at six different transects in LIS from a comprehensive survey in 1998. Seasonally averaged residual currents were laterally sheared and suggested strongly bathymetric influence. The lateral structure of residual currents from the three-dimensional simulations by Crowley (2005) for the same period showed good agreement with the major features in the observations of Vieira (2000). Comparisons emphasized the dependence of lateral current structure on lateral variations in channel depth.

Codiga and Aurin (2007) investigated the residual current structure at the far eastern end of LIS but outside of the main basin using long term ship-born ADCP

observations. Along the vessel transect, the along channel flow reveals a vigorous estuarine exchange circulation, with flow eastward out of the estuary in the upper water column of the southern half and inward westward movement strengthening with depth over the central and north section. Volume conservation implies that there is a strong eastward flow out of the estuary within the upper 7 m where no measurements were available.

There have been only a limited number of attempts to evaluate the relative strength of density-induced and tidally-induced residual currents within LIS. Wilson (1976) used a two-dimensional (vertical) model to evaluate the strength of density-induced circulation with the basin. His results were diagnostic in that they used hydrographic observations to infer the baroclinic pressure gradient, and they depended on a prescribed vertical eddy viscosity. Ianniello (1981) analyzed the longitudinal and vertical structure of tidally-induced residual currents in LIS using a two-dimensional analytical model for a rectangular channel of variable breadth and depth. As part of his analysis, he estimated the advective accelerations associated with the first order tidal current field, and found them to be of the same order as the baroclinic pressure gradient estimated by Wilson (1976) from hydrographic observations (1×10^{-5} ms^{-2} in the central basin). He concluded tidally-induced residual currents can be as important as density induced currents. Valle-Levinson and Wilson (1998) examined the effects of rotation and vertical mixing on volume exchange in eastern LIS by using a three-dimensional model. Results showed that the effects of rotation are to enhance recirculation and to reduce volume exchange. They also showed laterally sheared residual currents apparently dependent on bathymetry.

1.4 Objectives

In this study we perform three-dimensional numerical simulations in Long Island Sound as representative of wide estuary subject to strong semidiurnal tidal forcing as well as to significant longitudinal density gradients which maintain estuarine circulation. The three-dimensional numerical simulations offer the advantage of being able to incorporate the combined effects of baroclinicity associated with the longitudinal density gradient and advection, as well as the effects of stratification on vertical mixing. As part of these simulations we define three-dimensional structure of tidal currents and residual currents within the basin. The specific objectives were:

- To describe the tidal flow fields, to evaluate the tidal period longitudinal and lateral momentum balance, to test the barotropic scaling proposed by Winant (2007),
- To describe the residual flow fields, to evaluate the residual longitudinal and lateral momentum balance and to test the barotropic scaling proposed by Winant (2008) relevant to residual currents driven by tidal advection,
- To test the scaling proposed by Huijts et al (2008) concerning the relative strength of density driven and advectively driven residual currents.

Chapter 2

Methods and Model Description

2.1 Methods

The specific objectives outlined in Chapter 1.4 relate to a description of dynamics controlling the three-dimensional tidal and residual current structure in Long Island Sound. To meet these objectives we have exercised the three-dimensional primitive equation model ROMS (Shchepetkin and McWilliams, 2005) as previously applied to Long Island Sound by Crowley (2005). Crowley had as her objectives a description of the seasonal evolution of thermohaline circulation within the basin. This included a description of the three dimensional temperature and salinity fields, the heat and salt budgets for the basin, an analysis of longitudinal salt dispersion, and calculation of seasonal variations in the estuarine exchange flux.

Crowley (2005) focused on the specific period from April 1988 through September 1988 because of the availability of high quality data in connection with the US EPA funded Long Island Sound Study (LISS). These data provided time series for elevation as well as temperature and salinity on all open boundaries. These data provided meteorological observations from which surface heat and momentum fluxes could be obtained, and they provided temperature and salinity observations within the basin from which initial conditions could be derived. Bi-monthly temperature and salinity observations were also available throughout the basin interior; these data were assimilated and used for validation. In addition, complete daily-mean stream flow data for seven stations within the drainage basins of rivers discharging into LIS were available

from USGS. The model configuration and model skill are reviewed only briefly here. For details the reader is referred to Crowley (2005).

In this study we analyze the database representing the model output produced by Crowley (2005). Simulations have also been rerun using Crowley's (2005) grid and forcing fields to obtain momentum diagnostics (terms in the longitudinal and lateral momentum equations at selected sections).

2.2 Model configuration for Long Island Sound

The model domain extends from Throgs Neck in the west to Block Island in the east (Fig.1.1). ROMS uses orthogonal curvilinear coordinates in the horizontal and a stretched, terrain-following coordinate (sigma-coordinate) in the vertical. The grid developed by Crowley (2005) (Fig. 2.1) contains 42 by 352 cells with mean horizontal resolution of approximately 600 m, and 10 evenly spaced sigma-levels in the vertical. High-resolution bathymetry data extracted from the NOAA/NOS Geophysical Database were interpolated to the grid (Fig. 1.2).

The model was started from rest with initial temperature and salinity fields derived from LISS. Surface elevation was prescribed on the open boundaries from observations, and for the external mode, the depth-averaged velocities normal to the boundaries were calculated from the linearized momentum equations. An Orlanski radiation condition was applied to the internal-mode velocities, as well as to the tangential velocities in the external mode. Temperature and salinity at the open boundaries were weakly nudged toward observed values using an inflow-outflow condition with active and passive timescales of 1 day and 30 days, respectively.

ROMS uses a split-explicit time-stepping scheme; the time step used for this study was 6 s for the external mode and 120 s for the internal mode. A third-order upstream-biased advection scheme was used for both the momentum and tracer equations. The horizontal eddy viscosity coefficient, scaled by the grid spacing, had an average value of approximately 10 m^2 s^{-1} and no explicit horizontal tracer diffusivity was defined. The vertical eddy coefficients were calculated using a k-ω turbulence closure. A logarithmic formulation for the bottom stress was used with z_o = 0.01 m.

Beginning with Version 2.1, ROMS has a module which permits each term in the momentum and tracer equations to be saved, thereby permitting a detailed analysis of the time-evolving momentum and tracer balances.

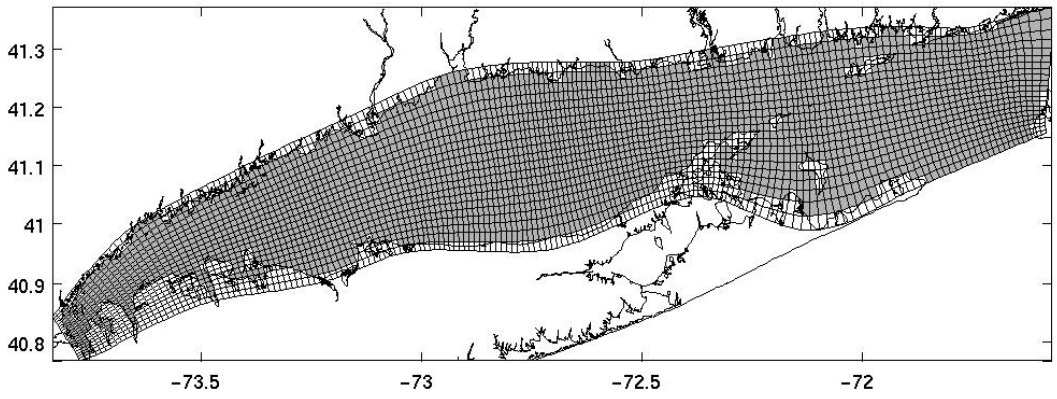

Figure 2.1. LIS model grid sub-sampled by a factor of two (Crowley (2005).

2.3 Model Skill

Table 2.1 lists observed and modeled values for the amplitude and phase lag (Greenwich epoch) for the five major tidal constituents at for NOS stations around LIS. The observed values for Bridgeport, New Haven and New London and Port Jefferson are published NOS constituents. The model reproduced the tidal amplitudes quite well, the differences between modeled and observed values being less than 0.05 m. However, the phase lags for the M_2 constituent for the model data are consistently smaller than those for the observations by as much as 10.5^o.

Correlations between modeled and observed surface and bottom values are shown in Fig. 2.2 for the LISS survey of 11–14 July, 1988. The correlation coefficients (R^2) are 0.81 and 0.73 for surface and bottom temperature, respectively, and 0.89 and 0.93 for surface and bottom salinity. The modeled temperature and salinity values show good agreement with the observations in the interior of LIS. Comparisons between CTD data and model profiles for temperature and salinity indicate that the thickness of the bottom mixed layer and the character of the surface intensified stratification are well represented in the model data.

Table 2.1. Observed and modeled elevation tidal constituents (Crowley 2005).

Station	Latitude	Longitude	Constituent	Observed		Modeled	
				Amplitude (m)	Epoch (^{o})	Amplitude (m)	Epoch (^{o})
Bridgeport	41.17	-73.18	M_2	0.991	109.6	1.008	101.8
			S_2	0.157	135.9	0.135	132.3
			N_2	0.200	87.6	0.182	88.2
			K_1	0.097	191.6	0.103	186.0
			O_1	0.064	219.5	0.061	214.7
New Haven Harbor	41.28	-72.91	M_2	0.862	106.0	0.910	97.1
			S_2	0.151	131.4	0.121	128.0
			N_2	0.195	80.8	0.165	82.7
			K_1	0.076	213.7	0.101	184.7
			O_1	0.094	211.6	0.060	213.9
New London	41.36	-72.09	M_2	0.372	58.3	0.406	50.4
			S_2	0.067	69.9	0.065	68.4
			N_2	0.087	34.6	0.085	31.4
			K_1	0.074	178.5	0.082	174.1
			O_1	0.053	209.0	0.049	204.5
Port Jefferson	40.95	-73.08	M_2	0.956	113.1	0.971	103.8
			S_2	0.155	139.9	0.131	134.7
			N_2	0.187	91.0	0.177	89.9
			K_1	0.091	192.4	0.100	187.1
			O_1	0.068	219.3	0.061	215.4

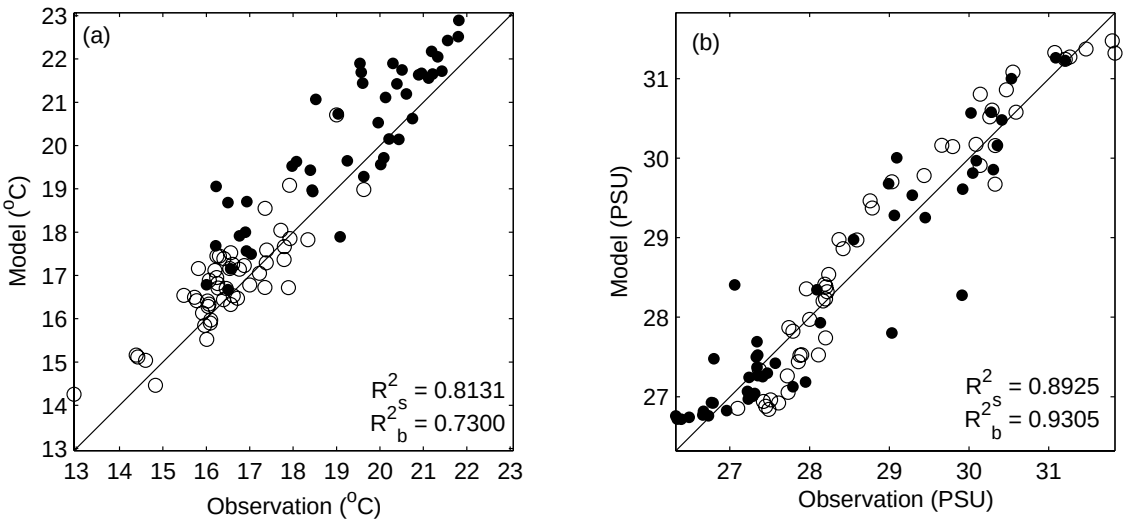

Figure 2.2. Correlation between modeled and observed surface (•, R^2_s) and bottom (○, R^2_b) values of (a) temperature and (b) salinity, 11–14 July 1988 (Crowley, 2005).

Chapter 3

Model Results: Three-Dimensional Tidal Flow

3.1 Sea level and depth mean tidal current

Figs. 3.1 and 3.2 show the M_2 amplitude and phase of sea level and depth mean longitudinal current in LIS from least squares analysis applied to model simulations from 05/11/88 to 07/30/88. Tidal range is seen to increase from approximately 0.4m in Block Island Sound (BIS) to 2m at the entrance to the East River, a signature of approximate quarter wave resonance. There is no significant lateral variation in the sea level amplitude. Sea level phase changes by approximately 110 degrees from BIS to the East River; phase throughout western LIS is nearly constant because of standing wave characteristics; the tide wave in eastern LIS is nearly progressive. There is some indication of phase advance along the north shore of the basin.

The amplitude of depth averaged longitudinal current (Fig. 3.2) shows significant longitudinal gradients, especially in the eastern end of the basin. Fig.3.3 shows the relationship between laterally averaged amplitude and the cross-sectional area. Ianniello (1981) hypothesized that advection associated with this longitudinal gradient in depth mean current would produce tidal residual currents within the basin. The phase of depth mean current indicates phase advance on the flanks of the basin.

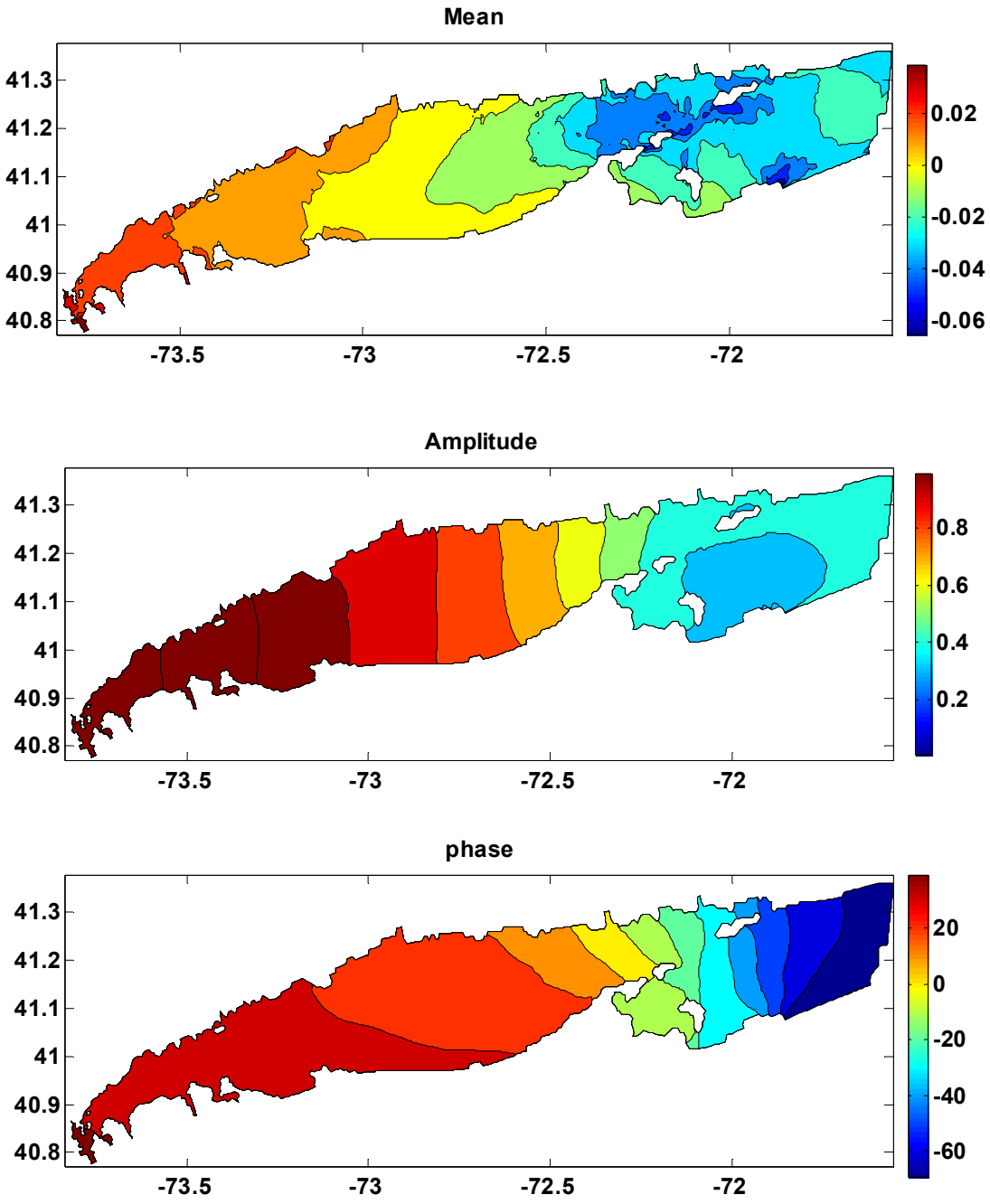

Figure 3.1. Mean (m), amplitude (m) and phase (degrees) of tidal range.

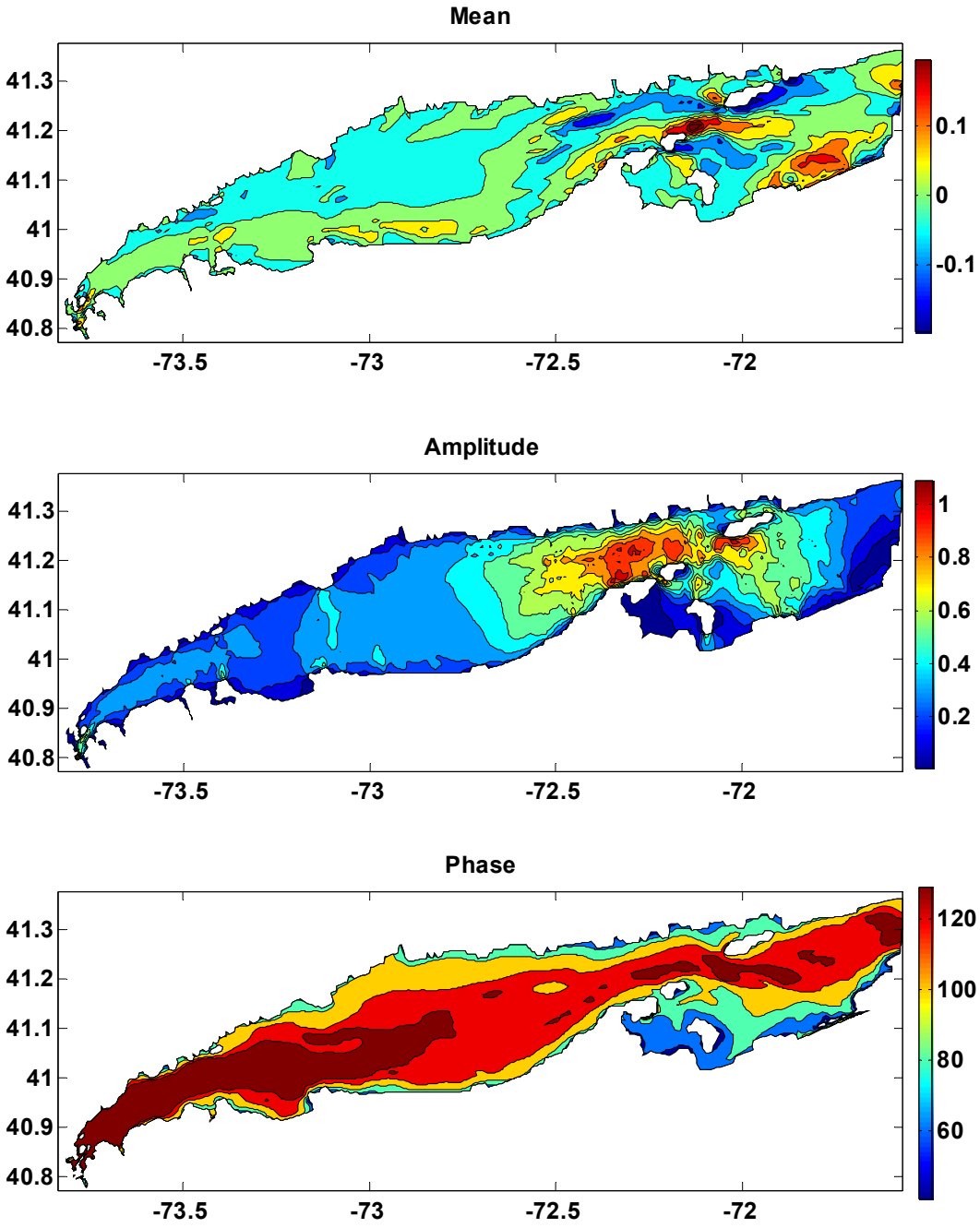

Figure 3.2. Mean (m/s), amplitude (m/s) and phase (degrees) of depth averaged longitudinal current.

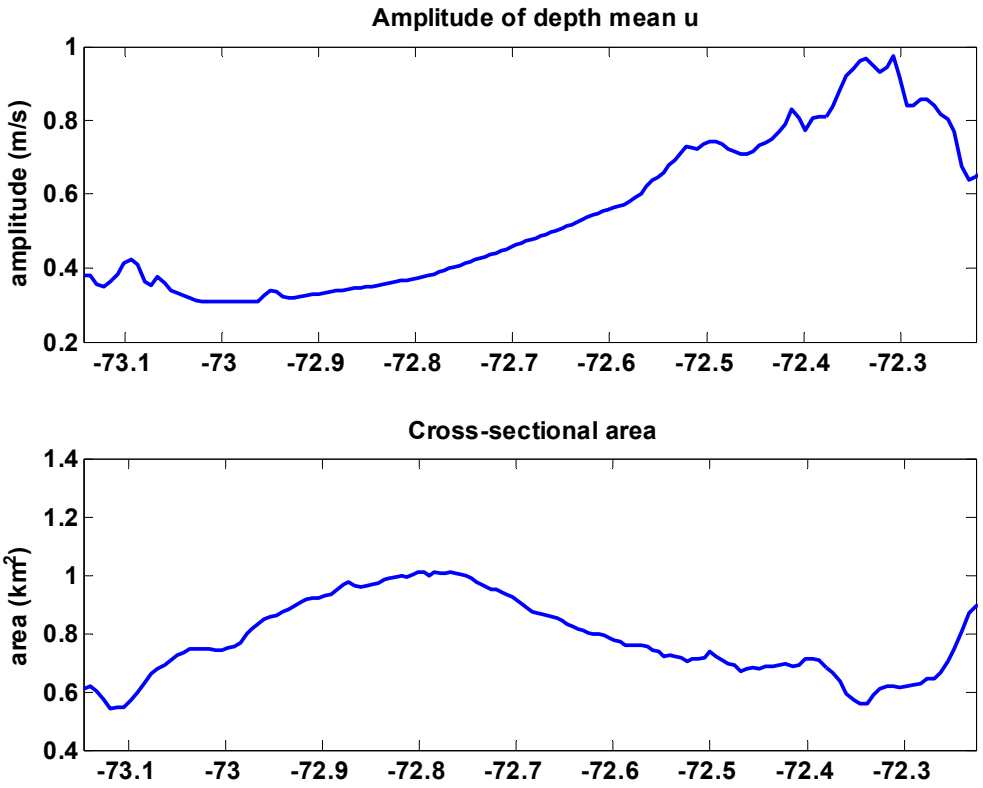

Figure 3.3. Laterally averaged amplitude for depth mean along channel current and cross-sectional area.

3.2 Three-dimensional velocity and density

Figs. 3.5-3.8 show tidal period variations in velocity and density for four lateral transects distributed over the basin interior from west to east located in Fig. 3.4. These particular transects were selected because they are distributed somewhat uniformly over the length of the basin and they avoid local bathymetry anomalies, also transect 113 corresponds with the ship-born ADCP transect. Note that each section is presented for an observer looking towards the western end of the basin. There are a number of characteristic features in the velocity structure represented at each section. These include a significant phase advance in longitudinal velocity near the bottom. Ebb velocities are

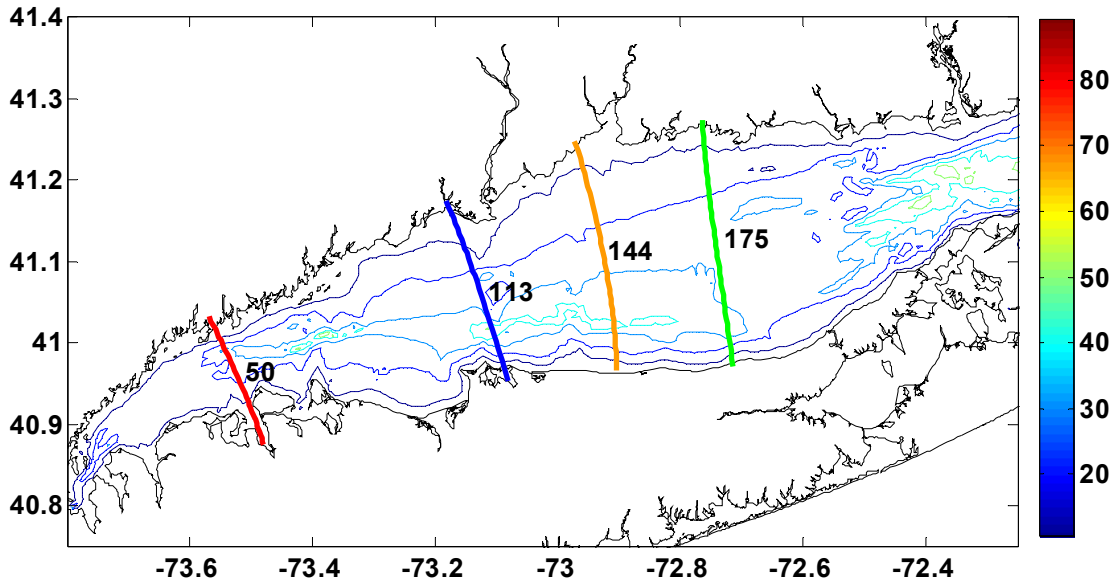

Figure 3.4. Locations of lateral transects at which velocity and density are presented (colorbar is depth in meters).

highly sheared; flood velocities are sheared as well but tend to exhibit a subsurface velocity maximum. These features are associated with the longitudinal baroclinic pressure gradient and the effects of straining of the density field on vertical mixing. More detail on the vertical structure in longitudinal velocity and the neap to spring variations is provided later. Longitudinal velocity also shows evidence for phase advance in shallow water.

Characteristic features in the lateral velocities at each section during late ebb include a counter-clockwise motion with surface velocities directed to the left and near bottom velocities towards the right. The lateral velocities exhibit a significant time lag relative to the longitudinal velocities. Characteristic features in the lateral velocities at each section during late flood include a clockwise motion.

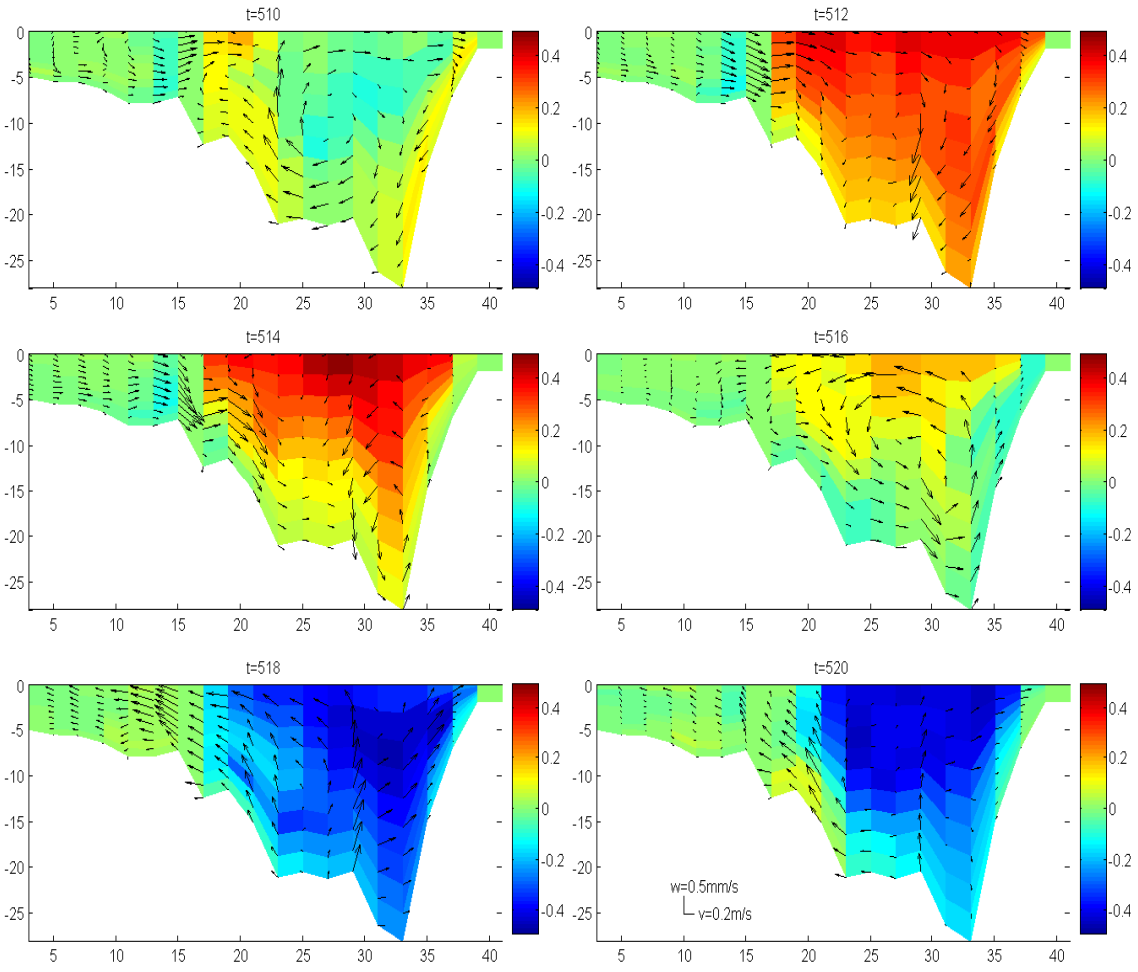

Figure 3.5. Tidal evolution of u (color), v,w (arrow) in m/s at transect 50 (scale of v, w in other subplots are same as subplot t=522, x-axis is the lateral grid number, t=510 to 522 indicates one tidal cycle on year day 152, spring tide.)

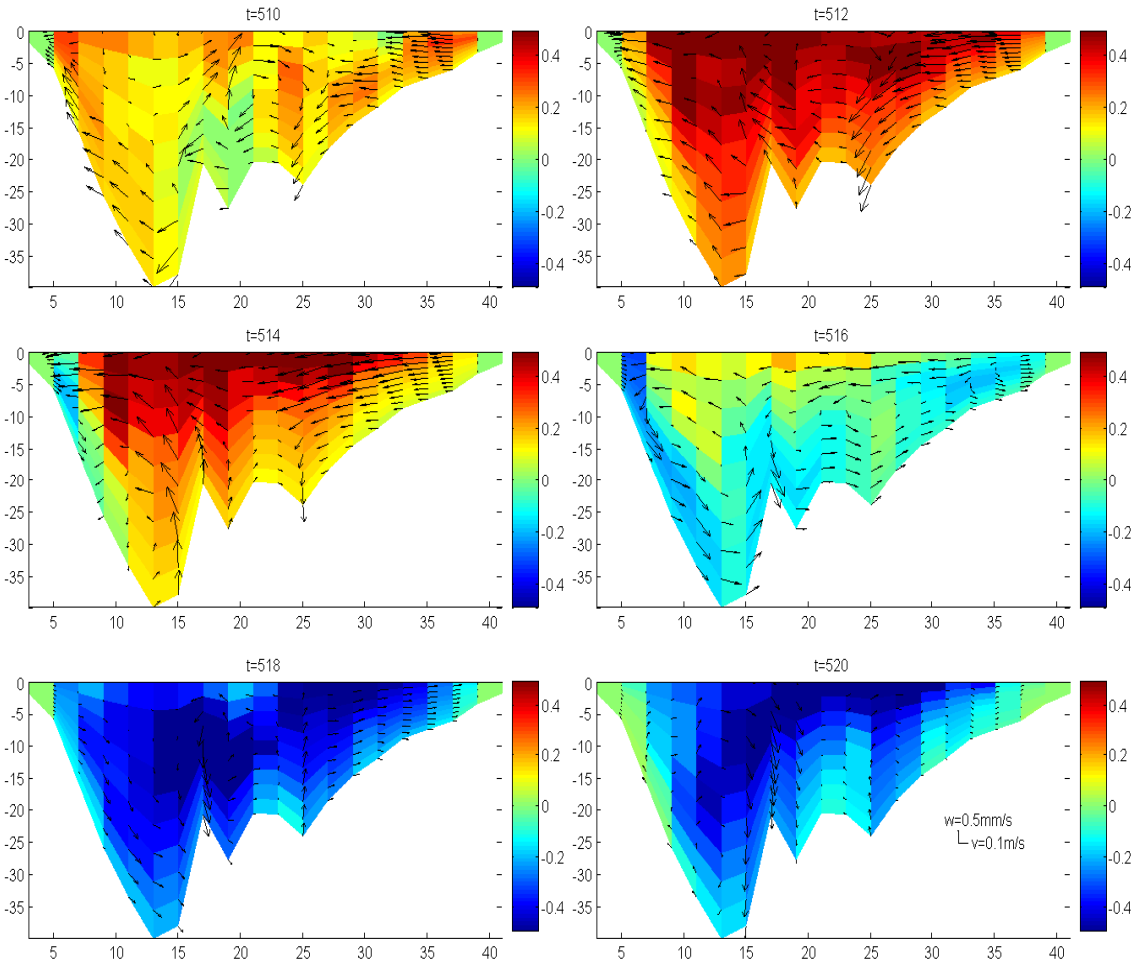

Figure 3.6. Tidal evolution of u (color), v,w (arrow) in m/s at transect 113 (scale of v, w in other subplots are same as subplot t=522, x-axis is the lateral grid number, t=510 to 522 indicates one tidal cycle on year day 152, spring tide.)

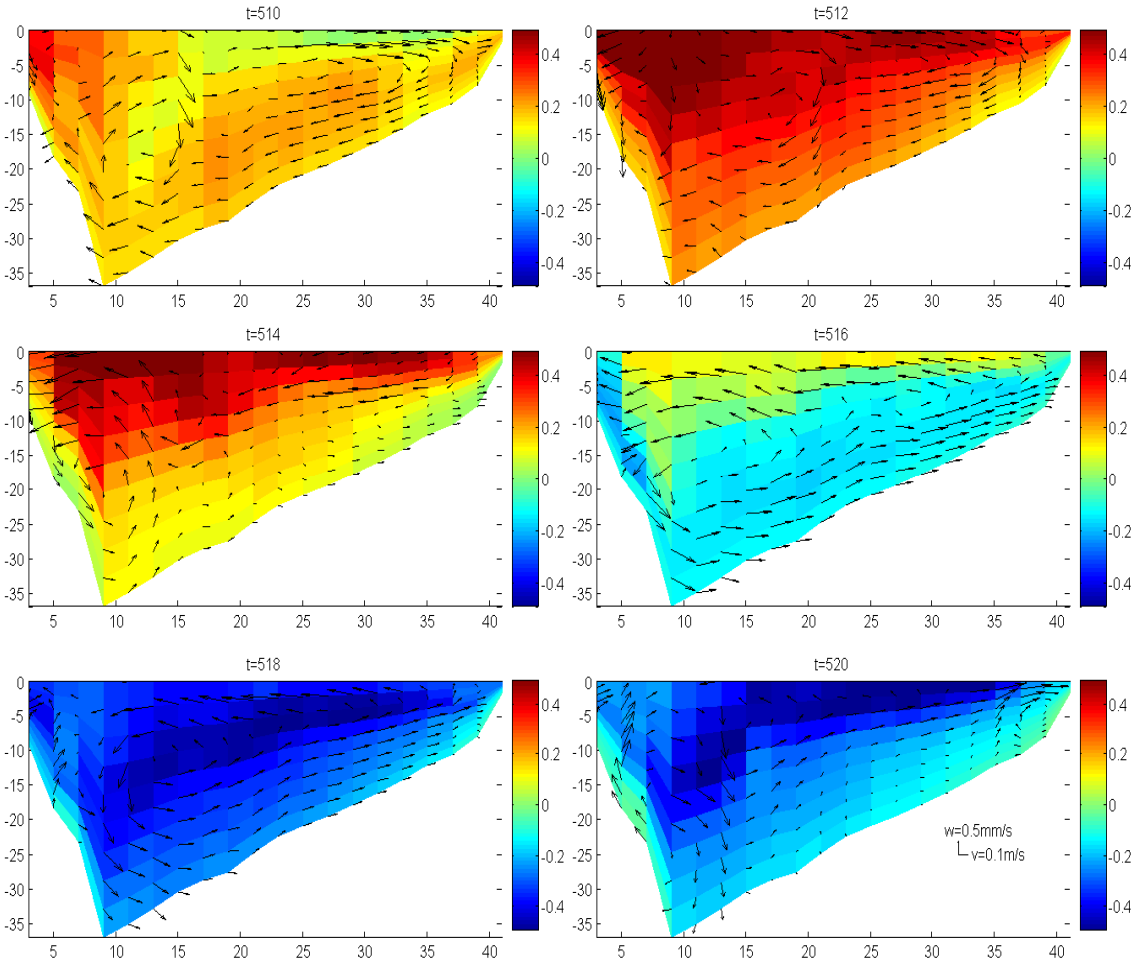

Figure 3.7. Tidal evolution of u (color), v,w (arrow) in m/s at transect 144 (scale of v, w in other subplots are same as subplot t=522, x-axis is the lateral grid number, t=510 to 522 indicates one tidal cycle on year day 152, spring tide.)

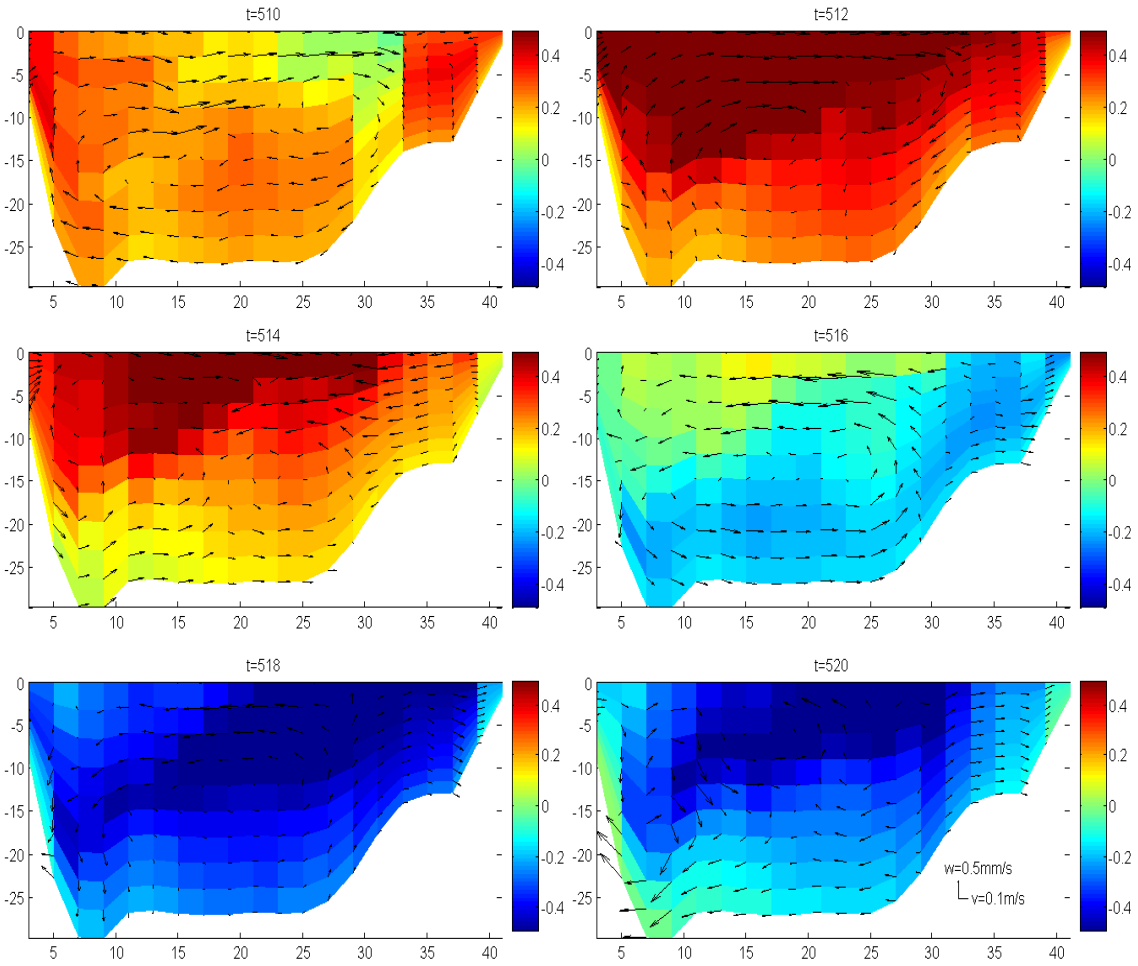

Figure 3.8. Tidal evolution of u (color), v,w (arrow) in m/s at transect 175 (scale of v, w in other subplots are same as subplot t=522, x-axis is the lateral grid number, t=510 to 522 indicates one tidal cycle on year day 152, spring tide.)

There are a number of characteristic features in the companion time series for density at each section (Figs. 3.9-3.12). Density was obtained from temperature and salinity but it reflects most strongly the salinity distribution. Each section shows a core of low temperature, high salinity and high density water in the channel. Density at each section show clear evidence for boundary mixing on the flanks which contributes to lateral density gradients. During flood, the bottom mixed layer tends to grow with some

sharpening of the halocline. During ebb, the stratification becomes somewhat more uniform because of straining of the density field by the velocity shear during ebb.

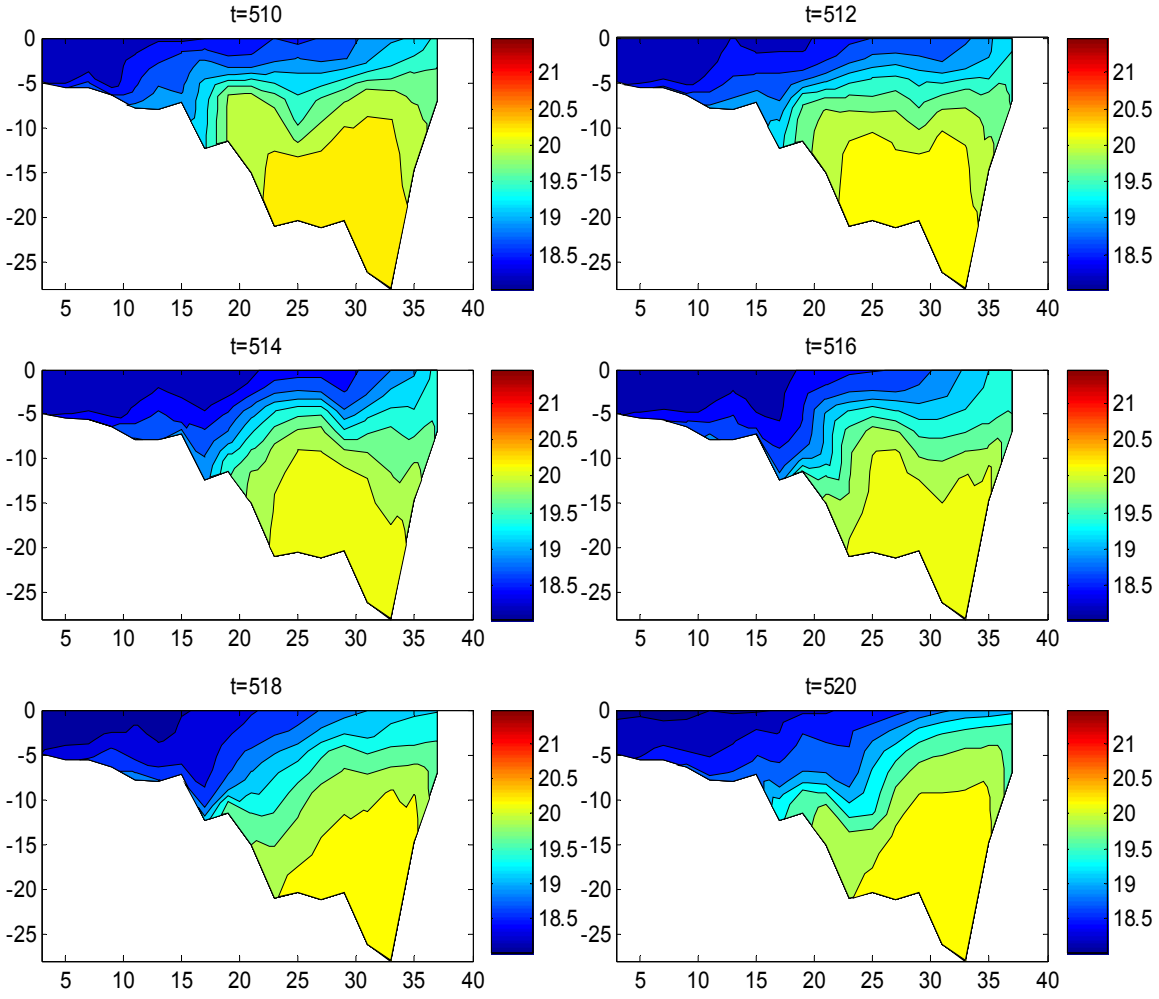

Figure 3.9. Tidal evolution of density (sigma-t) at transect 50

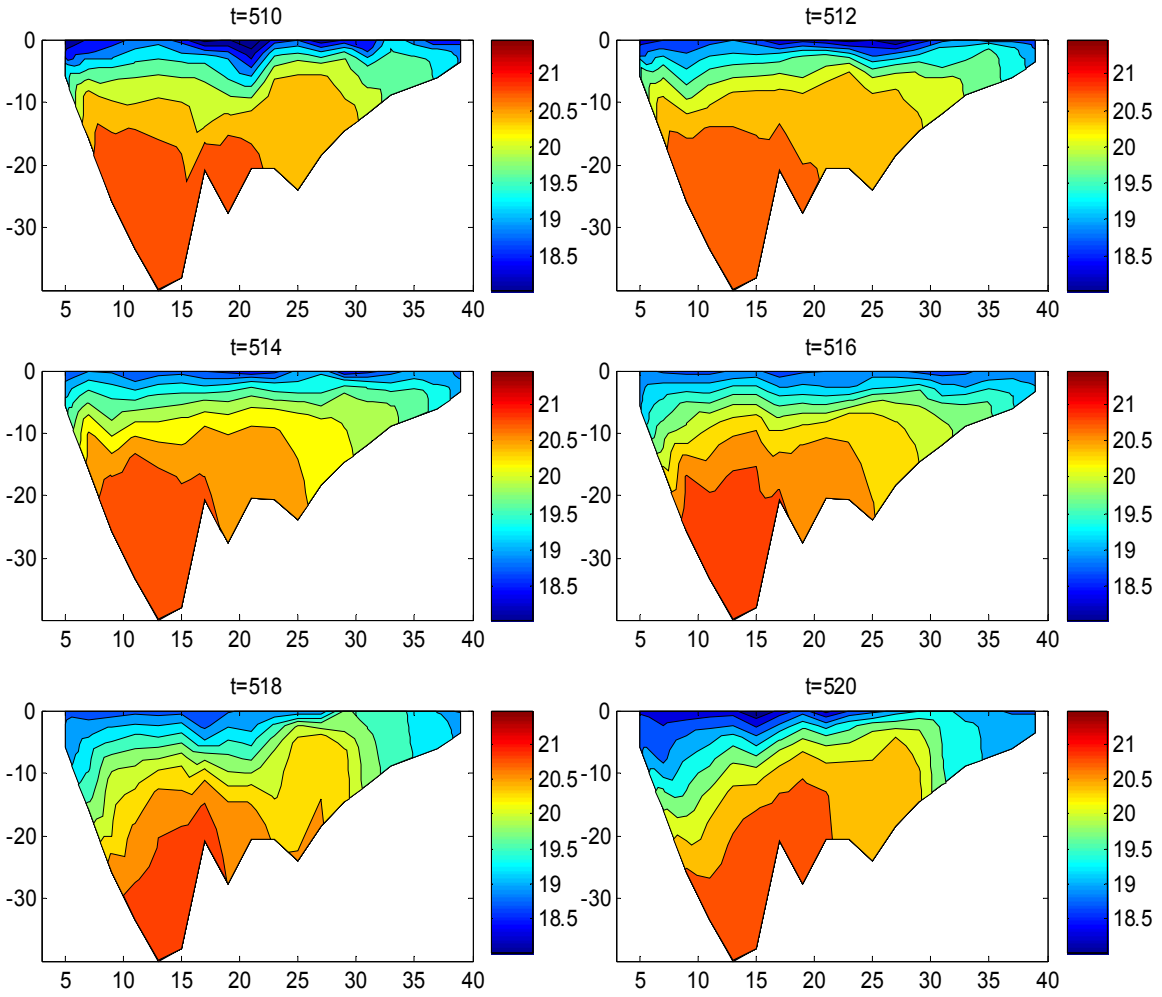

Figure 3.10. Tidal evolution of density (sigma-t) at transect 113

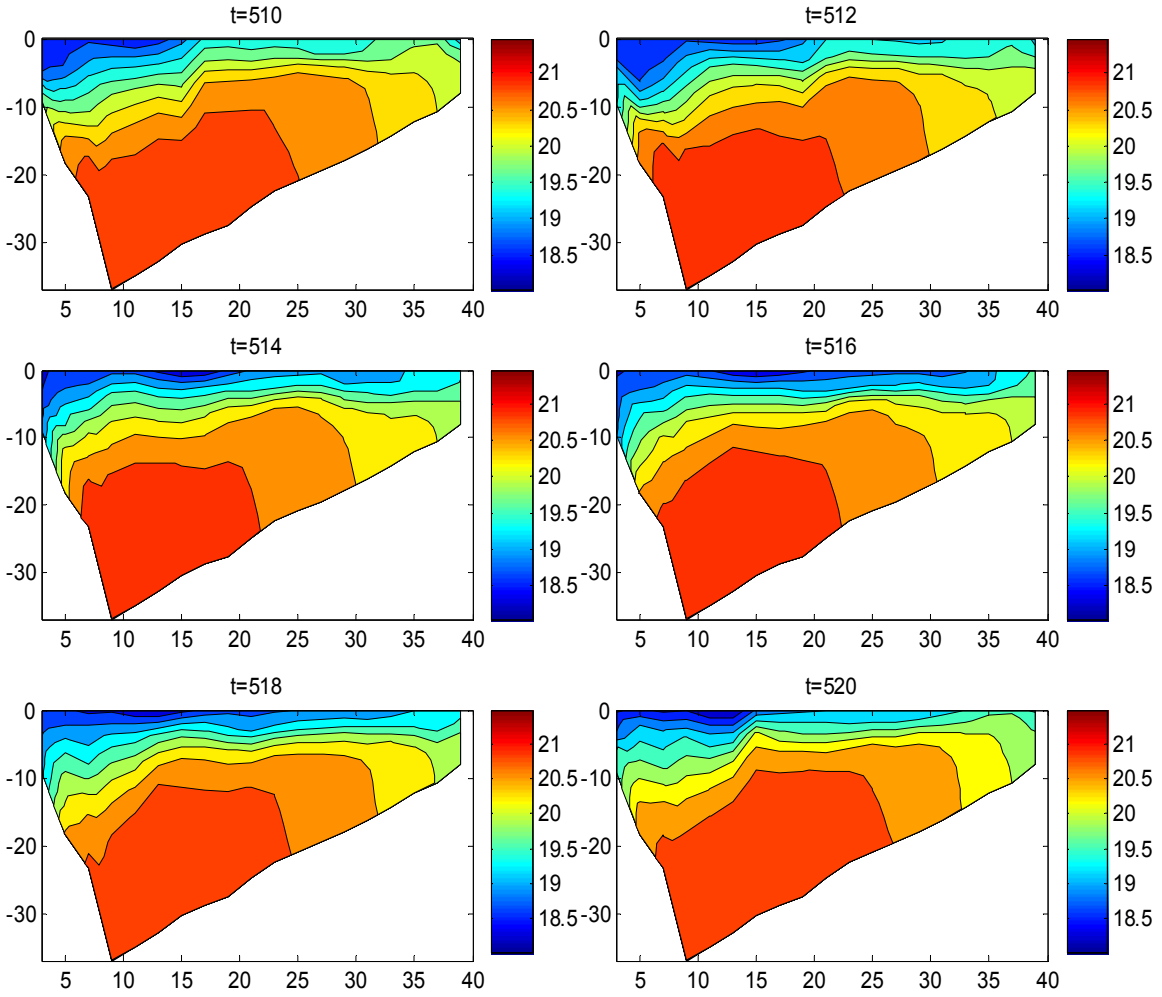

Figure 3.11. Tidal evolution of density (sigma-t) at transect 144

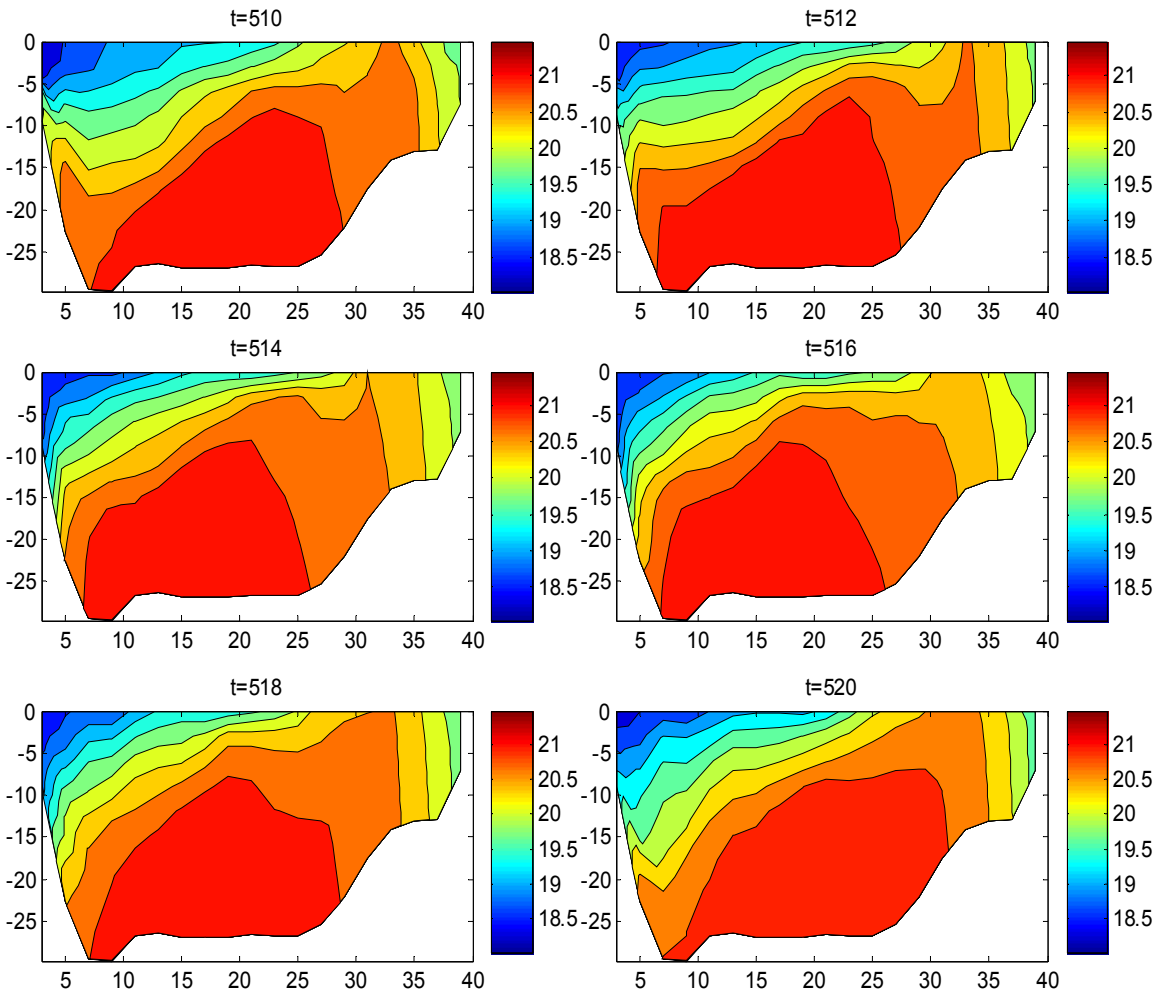

Figure 3.12. Tidal evolution of density (sigma-t) at transect 175

3.3 Longitudinal and lateral momentum balances

For a description of the tidal-period momentum balances contributing to the maintenance of the velocity structure discussed above, we focus on transect 144 because of the distinctive but relatively simple topography (Fig.3.13). Fig.3.14 shows the longitudinal momentum balance associated with the depth mean flow at station 13 in transect 144 for the time period of year day 148 to 149. It can be seen that acceleration is determined by pressure gradient. (Note that, here the pressure gradient refers to total

pressure gradient, but it is mainly barotropic, it is tested that depth-mean baroclinic pressure gradient is trivial during the tidal cycle). Friction is about one third of pressure gradient, which is relatively important compared to the other smaller terms. The companion lateral momentum balances shown in Fig. 3.15 indicate essentially a geostrophic balance, explained by the primary balance between pressure gradient and Coriolis force, and all the other terms are equally small.

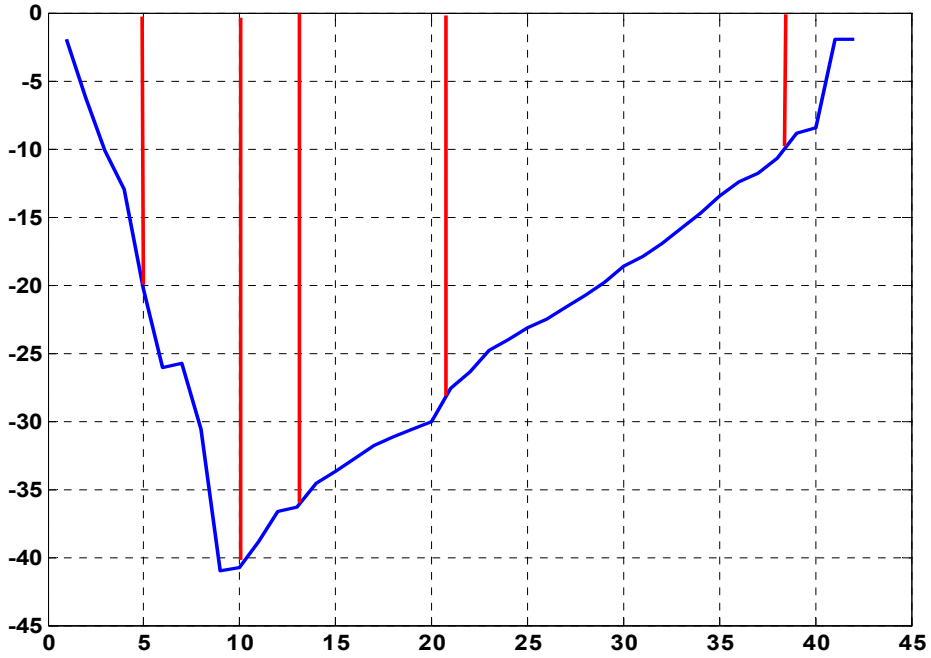

Figure 3.13. Bathymetry at transect 144 and lateral positions of stations discussed in text.

The standard deviations of the terms shown in Figs. 3.14 and 3.15 are plotted in Figs. 3.16 and 3.17, respectively. These standard deviations confirm that the longitudinal momentum balance is primarily between local acceleration, pressure gradient and friction across the entire section with increased frictional contribution in shallow water. They also confirm that the lateral balance is geostrophic across the section.

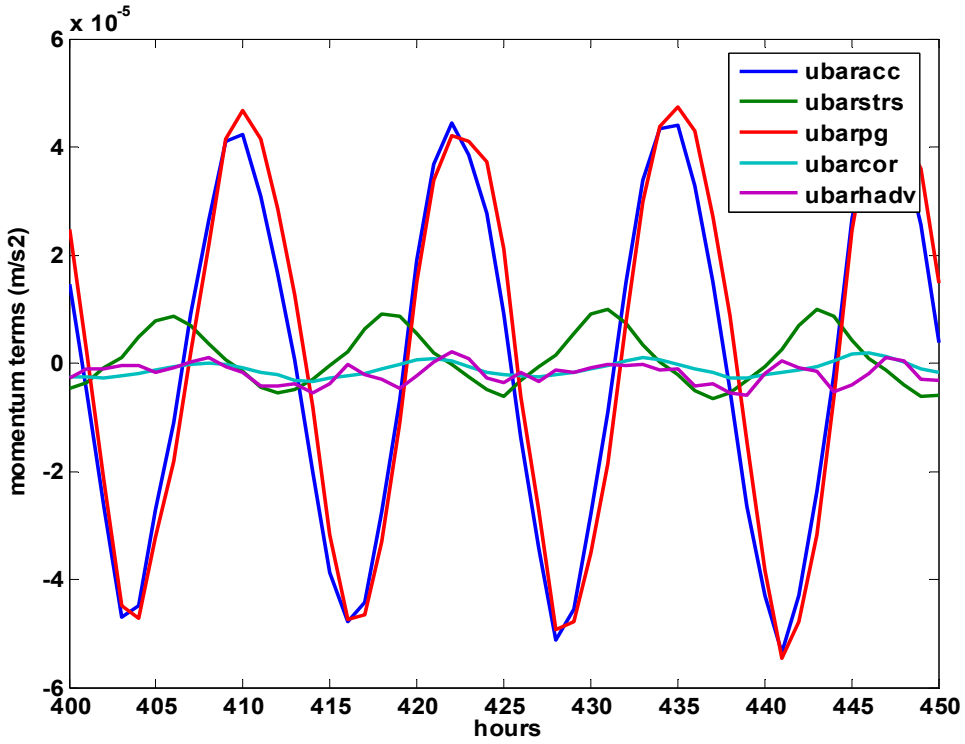

Figure 3.14. Longitudinal momentum balance associated with depth mean flow at station 13, transect 144.

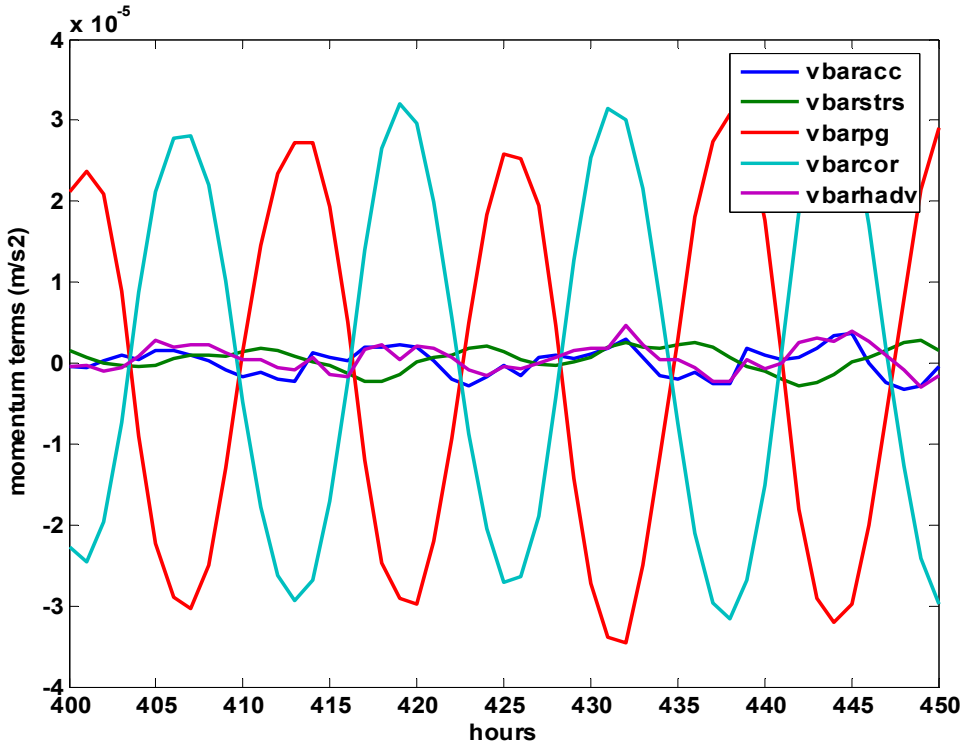

Figure 3.15. Lateral momentum balance associated with depth mean flow at station 13, transect 144.

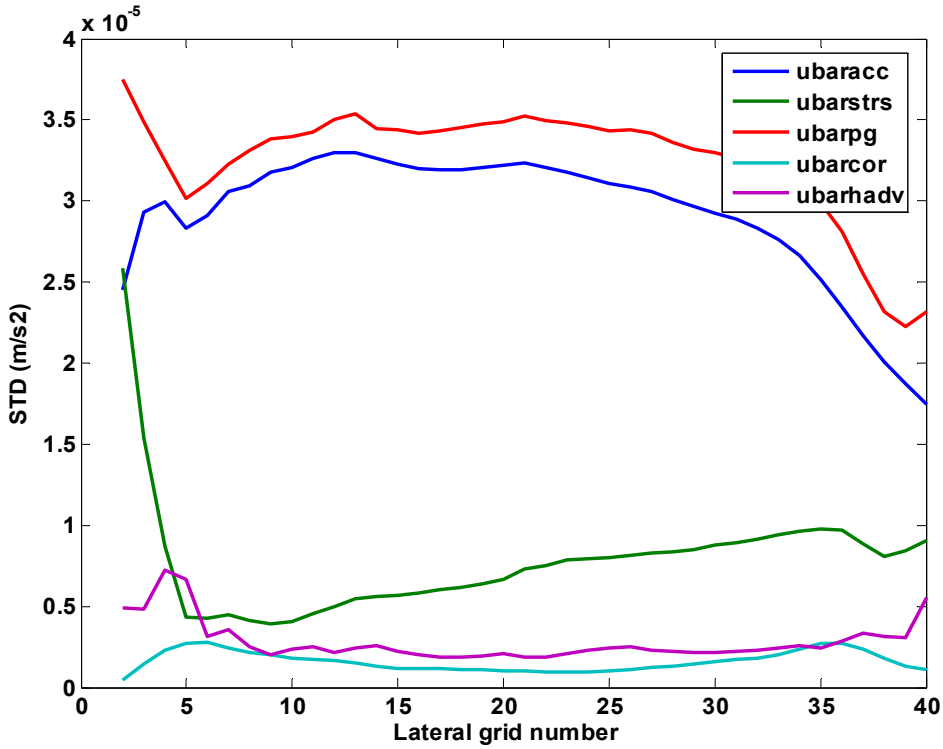

Figure 3.16. Standard deviations of terms in longitudinal momentum balance associated with depth mean flow at transect 144.

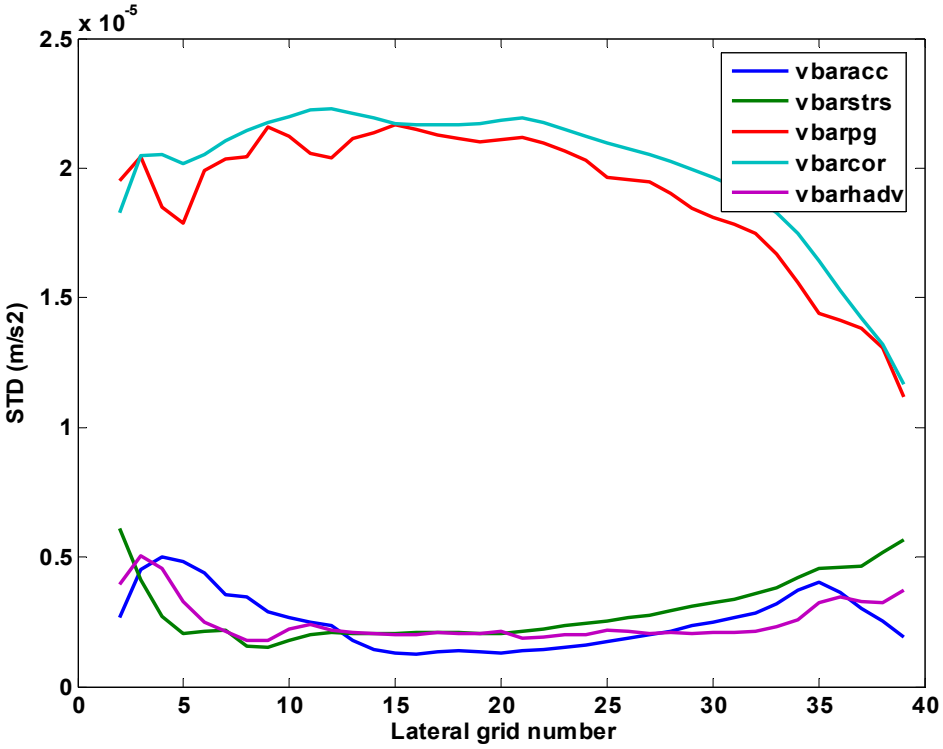

Figure 3.17. Standard deviations of terms in lateral momentum balance associated with depth mean flow at transect 144.

Figs.3.18-3.20 provide a description of the longitudinal momentum balance associated with the three-dimensional motion. They show time series of the terms in the longitudinal momentum equation at station 21 in transect 144 for the period of year day 154 to 156 for three sigma levels. Note that these simulations were for ten equally sized sigma levels with level 10 being the upper most level, and that the mean tidal level (MTL) depth at station 21 is approximately 27.5 m. Included with these momentum plots is a plot of longitudinal and lateral velocity to show phase relationships.

At sigma level 9 in the upper water column (Fig. 3.18), the primary momentum balance is between local acceleration and barotropic pressure gradient. Figs. 3.19 and 3.20 show that this balance is maintained further down in the water column but with increasing contribution from friction (stress divergence).

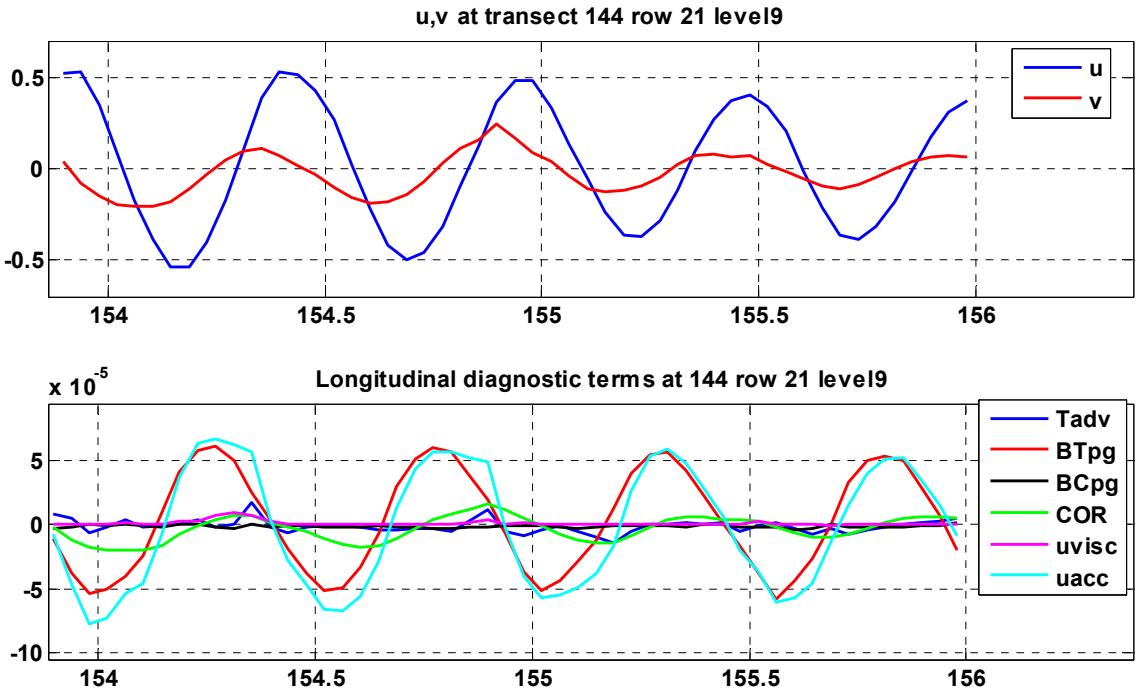

Figure 3.18. Time series for terms in the longitudinal momentum balance at sigma level 9, station 21, transect 144. (Tadv: Total advection; BTpg: Barotropic pressure gradient; BCpg: Baroclinic pressure gradient; COR: Coriolis; uvisc: friction; uacc; acceleration).

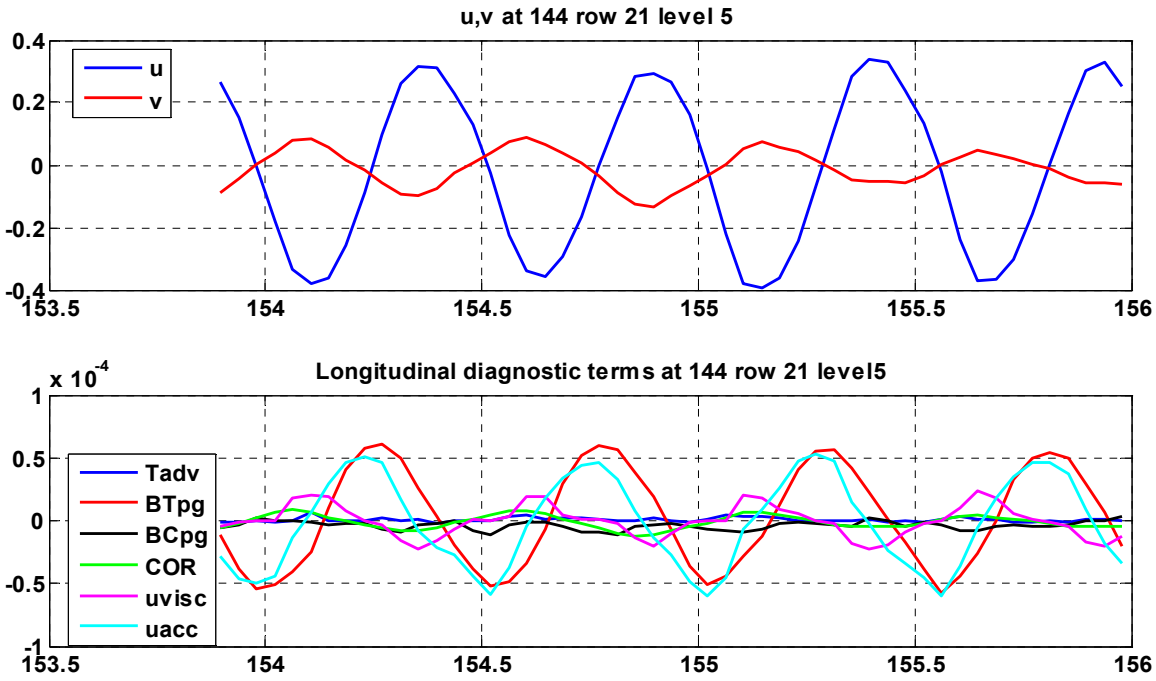

Figure 3.19. Time series for terms in the longitudinal momentum balance at sigma level 5, station 21, transect 144.

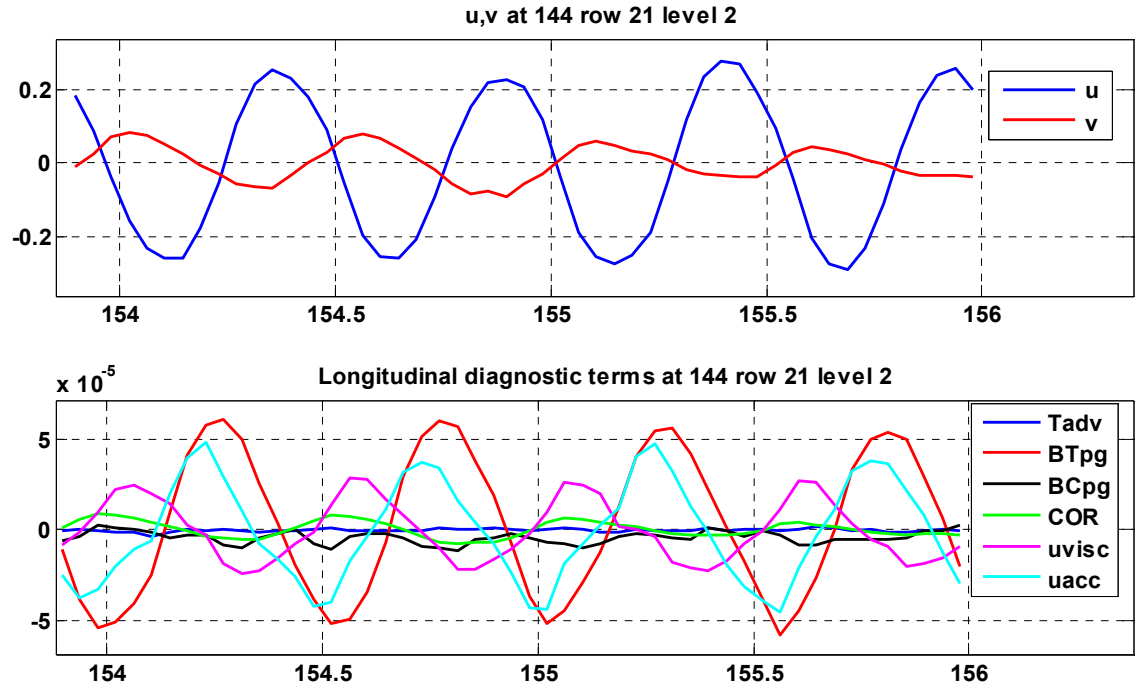

Figure 3.20. Time series for terms in the longitudinal momentum balance at sigma level 2, station 21, transect 144.

Fig. 3.21 shows the standard deviations of the terms in the longitudinal momentum balance as a function of sigma level at station 21, transect144. The primary longitudinal balance is seen to be between barotropic pressure gradient and local acceleration, with an increasing and significant contribution from friction at depth. There is also some contribution from Coriolis acceleration in the upper water column. Both advection and baroclinic pressure gradient are relatively small in the tidal cycle.

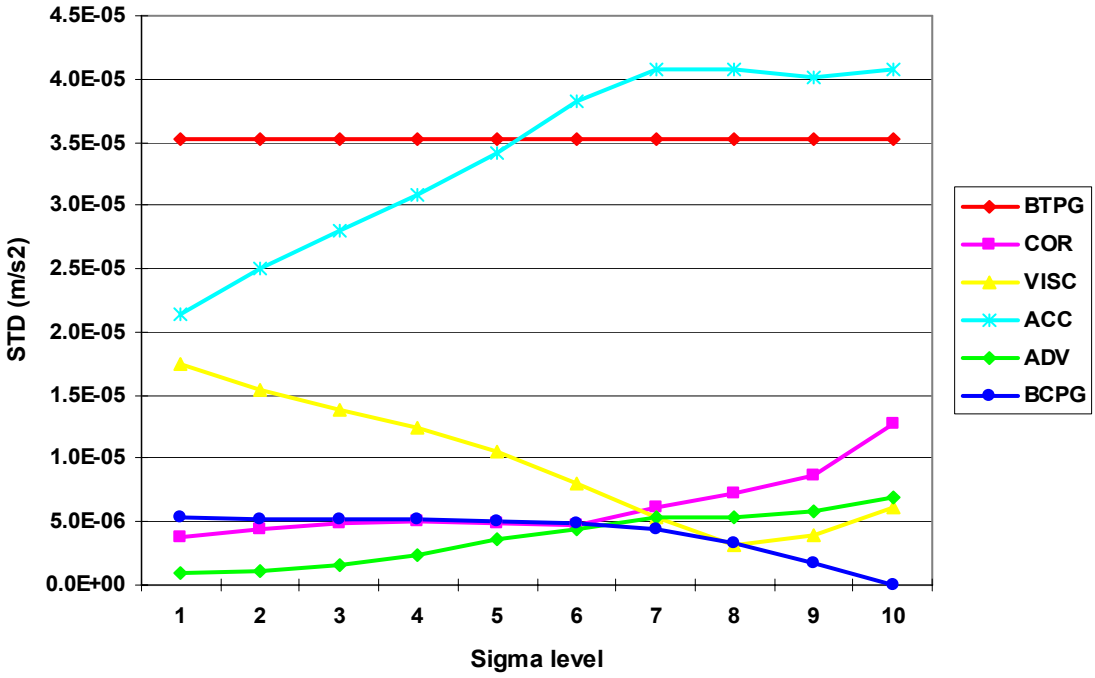

Figure 3.21. Standard deviations for terms in the longitudinal balance as a function of sigma level at station 21, transect 144 (level 10 is surface).

Figs. 3.22-3.24 provide a description of the companion lateral momentum balance associated with the three-dimensional motion at the same location and time period as shown in Figs. 3.18-3.20. At sigma level 9 in the upper water column (Fig. 3.22), the primary momentum balance is between Coriolis acceleration and barotropic pressure

gradient, with the Coriolis acceleration exceeding the pressure gradient to produce the local acceleration. At sigma level 5 in the center of the water column (Fig. 3.23), the primary momentum balance is also between Coriolis acceleration and barotropic pressure gradient, but the Coriolis acceleration and the pressure gradient are nearly in balance with some additional contribution from stress divergence. In the bottom of the water column (Fig. 3.24), the primary momentum balance is still between Coriolis acceleration and barotropic pressure gradient, but the pressure gradient is significantly greater than the Coriolis acceleration (reverse to the surface), again with some contribution from stress divergence.

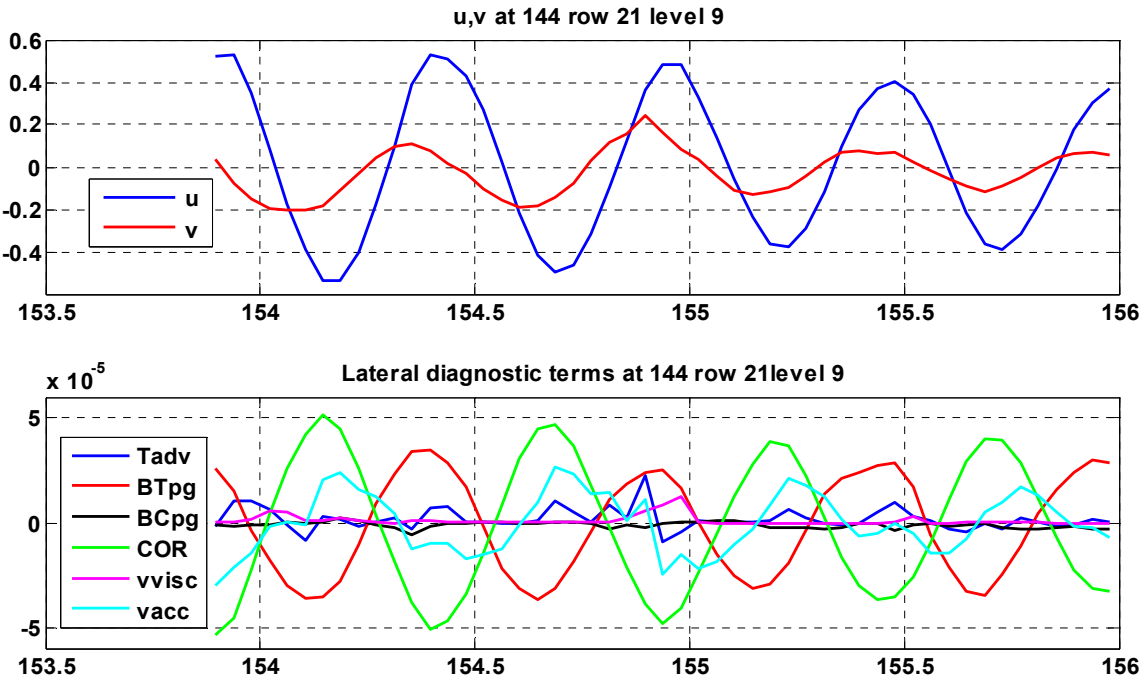

Figure 3.22. Time series for terms in the lateral momentum balance at sigma level 9, station 21, transect 144.

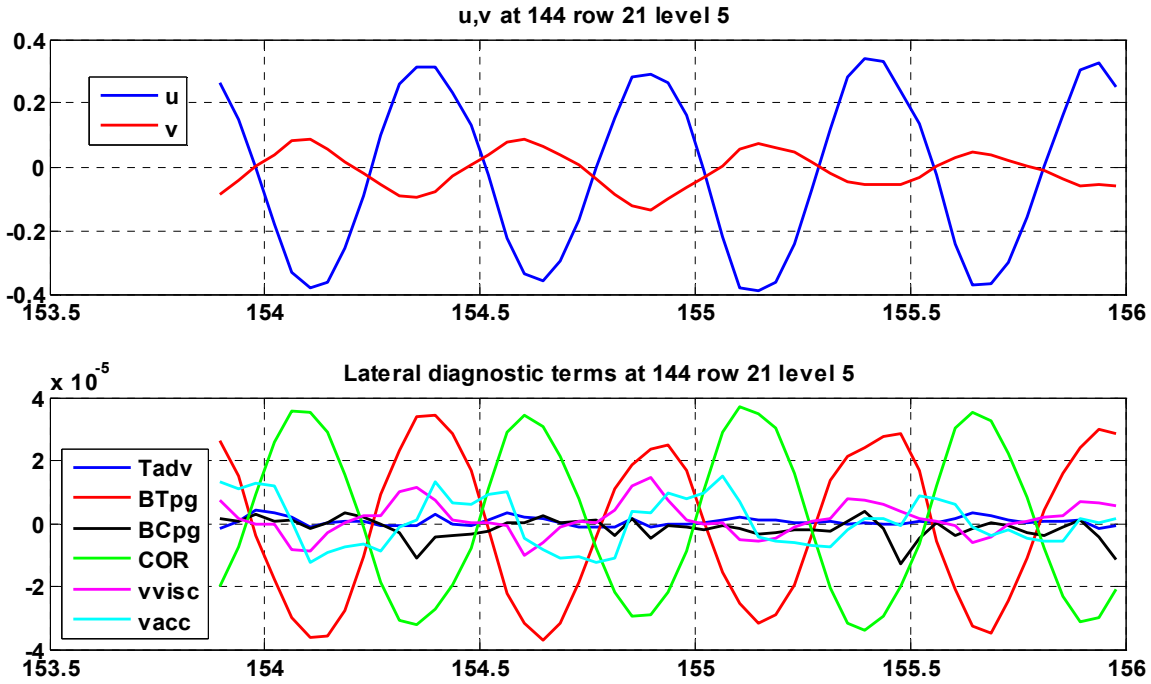

Figure 3.23. Time series for terms in the lateral momentum balance at sigma level 5, station 21, transect 144.

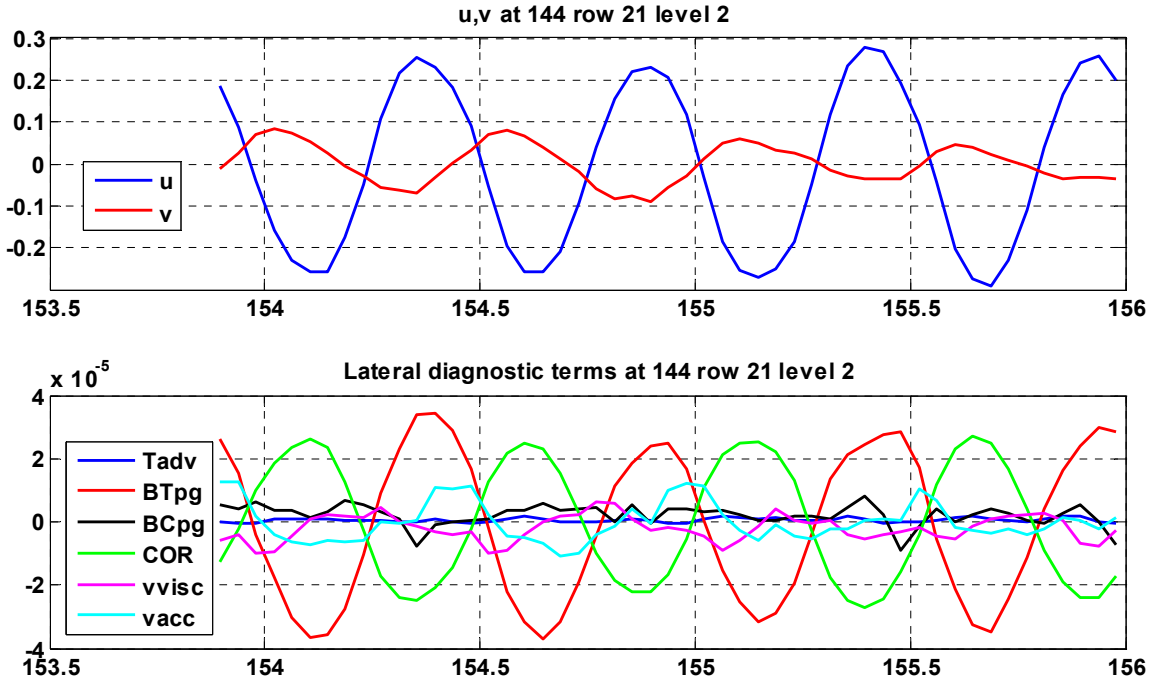

Figure 3.24. Time series for terms in the lateral momentum balance at sigma level 2, station 21, transect 144.

Insight into the details of tidal variations in vertical shear in longitudinal tidal currents at transect 144 responsible for the depth dependent lateral momentum balance described above is provided by Fig. 3.25. During flood a strong shear exists beneath the halocline; above the halocline shear is weak or reversed. During ebb shear is relatively uniform with depth. At column 21 near the deeper part of the transect, this vertical structure is preserved from neap tide to spring tides, but with a significant increase in shears during spring tides. At column 38 on the shallow northern flank (note the change in depth scale) of transect 144, this same vertical structure is seen during neap tides, with shears significantly reduced from those seen at column 21. During spring tides there is evidence that the halocline reaches nearly to the surface.

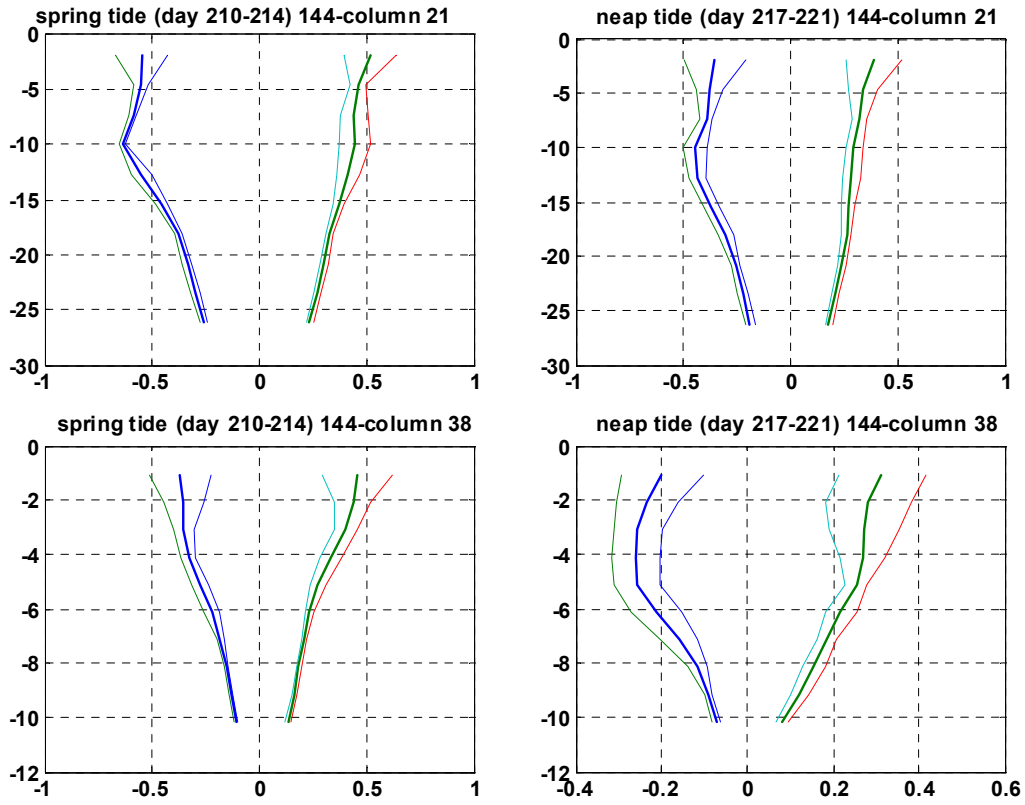

Figure 3.25. Vertical structure of phase averaged longitudinal currents at columns 21 and 38 in transect 144 (see Fig. 3.13).

Fig. 3.26 shows the standard deviations of the terms in the lateral momentum balance as a function of sigma level at station 21, transect144. The primary lateral balance is seen to be between barotropic pressure gradient and Coriolis acceleration. In the upper water column Coriolis acceleration exceeds barotropic pressure gradients, which contributes to local acceleration. In the lower water column barotropic pressure gradient exceeds Coriolis acceleration with additional contribution from lateral baroclinic pressure gradient and stress divergence. Advection is not significant in this lateral balance.

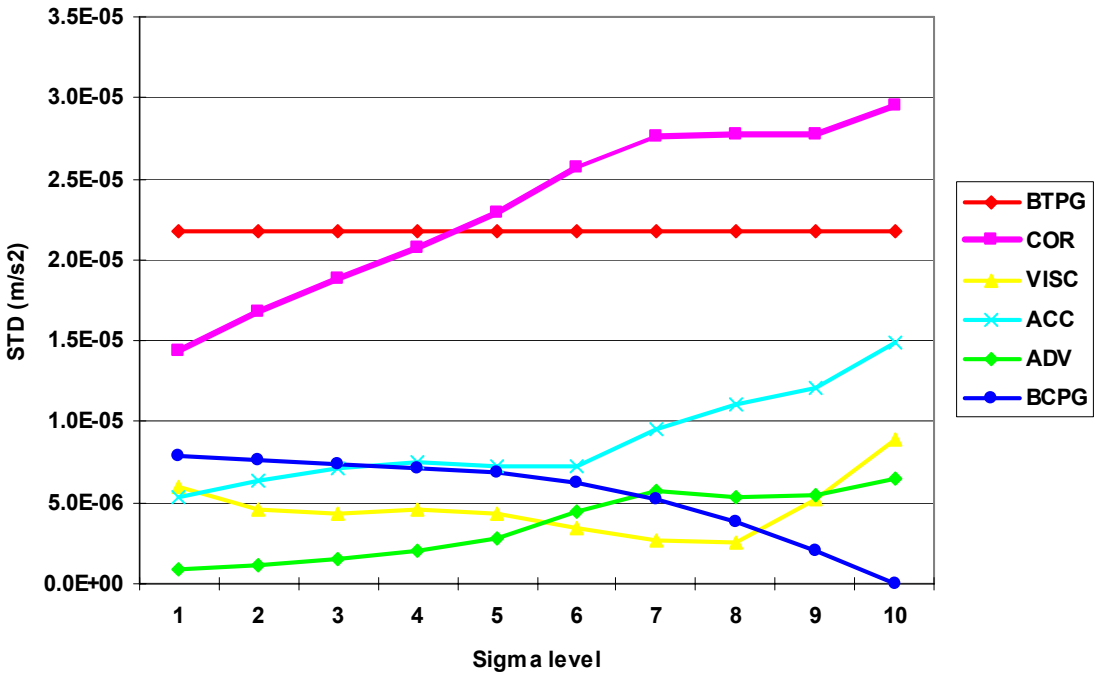

Figure 3.26. Standard deviations for terms in the lateral balance as a function of sigma level at station 21, transect 144.

3.4 Discussion

A useful framework for interpreting the momentum balances and flow structure described above is provided by the analytical model developed by Winant (2007) for the three-dimensional structure of barotropic tidal currents in an elongated co-oscillating basin. His model depends on five non-dimensional parameters: two of these, including the basin aspect ratio $\alpha=B/L$, and friction parameter $\delta=(2K/\omega H^2)^{1/2}$, which is the ratio of the amplitude of the periodic boundary layer thickness to water column depth, were mentioned in Chapter 1. The three additional parameters include: 1) the ratio of the amplitude of the tidal wave at the open boundary to the depth $\varepsilon=C/H$ where C is the amplitude and H is maximum channel depth, 2) the ratio of the inertial frequency to the angular tidal frequency $f=f/\omega$, and 3) the ratio of basin length to tidal wavelength $\kappa=\omega L/\sqrt{(gH)}$ $(\times 2\pi)$. Winant's (2007) scaling $x=x^*/L^*$, $y=y^*/B^*$, where x^* and y^* are dimensional longitudinal and lateral coordinates, and the continuity inferred scaling $u=u^*/(\varepsilon\omega L^*)$, $v=v^*/(\varepsilon\omega B^*)$ where u^* and v^* are dimensional longitudinal and lateral velocities, leads to fundamentally different longitudinal and lateral momentum balances (for small ε) :

$$\begin{aligned}\frac{\partial u}{\partial t} &= f\alpha v - \frac{1}{\kappa^2}\frac{\partial \eta}{\partial x} + \frac{\delta^2}{2}\frac{\partial^2 u}{\partial z^2} \\ \frac{\partial v}{\partial t} &= -\frac{f}{\alpha}u - \frac{1}{\alpha^2\kappa^2}\frac{\partial \eta}{\partial x} + \frac{\delta^2}{2}\frac{\partial^2 v}{\partial z^2}\end{aligned} \qquad (3.1)$$

Figs. 3.21 and 3.26 allow us to test the relevance of this barotropic scaling to tidal current structure in LIS. Estimates for the magnitudes of the parameters for LIS are: $\varepsilon \sim 0.05$, $\alpha \sim 0.25$, $\delta \sim 0.5$, $f \sim 0.67$, and $\kappa \sim 1.57$. For these parameter values we obtain

estimates for coefficients $f\alpha$, $1/\kappa^2$, and $\delta^2/2$ in the longitudinal momentum equation of 0.1, 0.4, and 0.1, respectively. If we assume that the local acceleration in the longitudinal momentum equation is of order 1, then the dominant balance is between barotropic pressure gradient and local acceleration. This is consistent with the ratio of terms in Fig. 3.21. We obtain estimates for coefficients f/α, $1/\alpha^2\kappa^2$, and $\delta^2/2$ in the lateral momentum equation of 3, 6, and 0.1, respectively. If we assume that the local acceleration in the lateral momentum equation is of order 1, then the dominant balance is between barotropic pressure gradient, Coriolis acceleration and local acceleration, which is consistent with the ratio of terms in Fig. 3.26.

It is also interesting to note that Winant (2007) obtained a result for the amplitude and phase of $\alpha V/fU$, the ratio of α times the dimensional lateral velocity to f times the dimensional axial velocity as a function of δ and f. For our values of α and f, this gives an amplitude ratio of 0.3, in excellent agreement with our M_2 least squares results applied to axial and lateral velocities, and a phase which is consistent with our calculated $\pi/2$ phase lag between lateral and axial flow near the surface (Fig. 3.27) .

We conclude that the barotropic scaling proposed by Winant (2007) is consistent with tidal period longitudinal and lateral momentum balances in LIS, that tidal period lateral motion is produced primarily by Coriolis forcing rather than differential advection or boundary mixing. We also conclude that this Coriolis forced lateral motion will contribute to the maintenance of tidal residual motion in the basin.

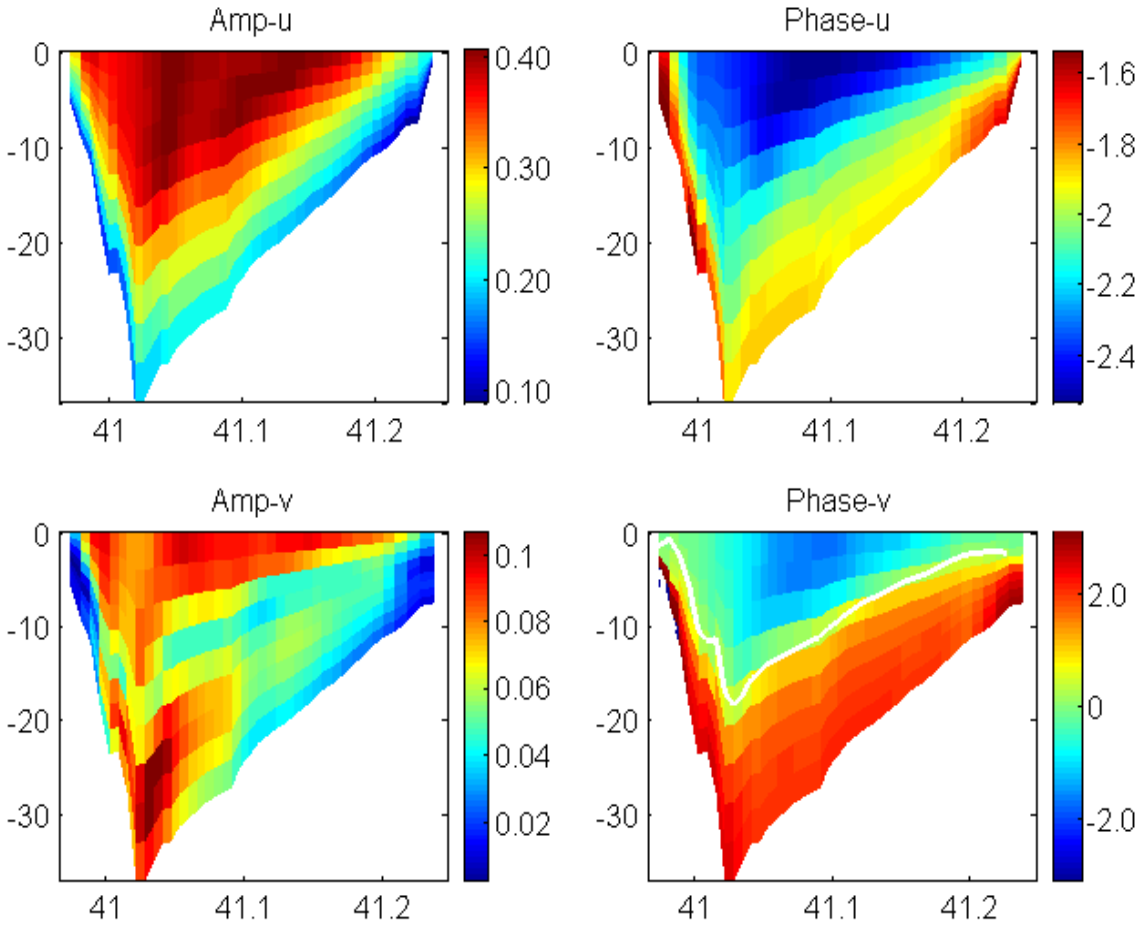

Figure 3.27. M2 amplitude and phase of axial and lateral velocity at transect 144.

Chapter 4

Model Results: Three-Dimensional Residual Flow

4.1 Mean sea level

Fig. 4.1 shows mean sea level in LIS obtained from model simulations for the period 05/11/88 to 07/30/88. It emphasizes the longitudinal and lateral sea level gradients which contribute to the residual barotropic pressure gradient. The Longitudinal variation in mean sea level along three model grid rows near the center of the channel (Fig. 4.2) indicates that the longitudinal barotropic pressure gradient is directed seaward and is relatively uniform over the western and central part of the basin. There is a significant increase in the seaward directed pressure gradient in the eastern part of the basin. The longitudinal barotropic pressure gradient balances the sum of the vertically integrated advection, baroclinic pressure gradient, Coriolis acceleration and stress divergence. Within the eastern and central basin, the lateral barotropic pressure gradient is directed towards the south along the north side of the basin, and towards the north along the south side of the basin.

4.2 Three-dimensional residual current fields

Three-dimensional residual Eulerian current field in LIS has never been adequately described. The flow patterns developed by Vieira (2000) in light of moored current observations remain the most contemporary description to date. Figs. 4.3-4.5 show residual Eulerian currents at three sigma levels defined from model simulations for

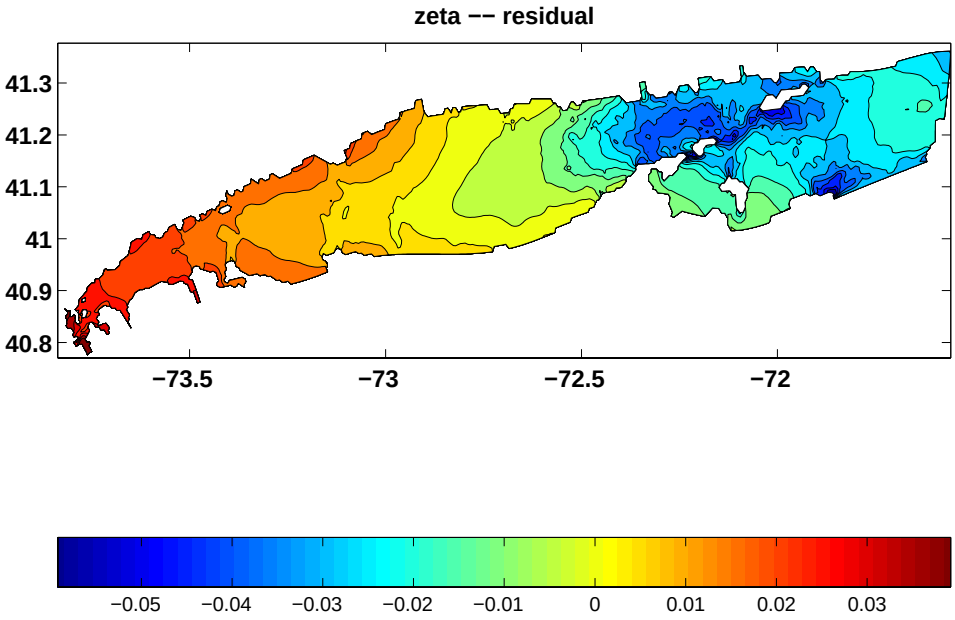

Figure 4.1. Spatial variations in mean sea level (m).

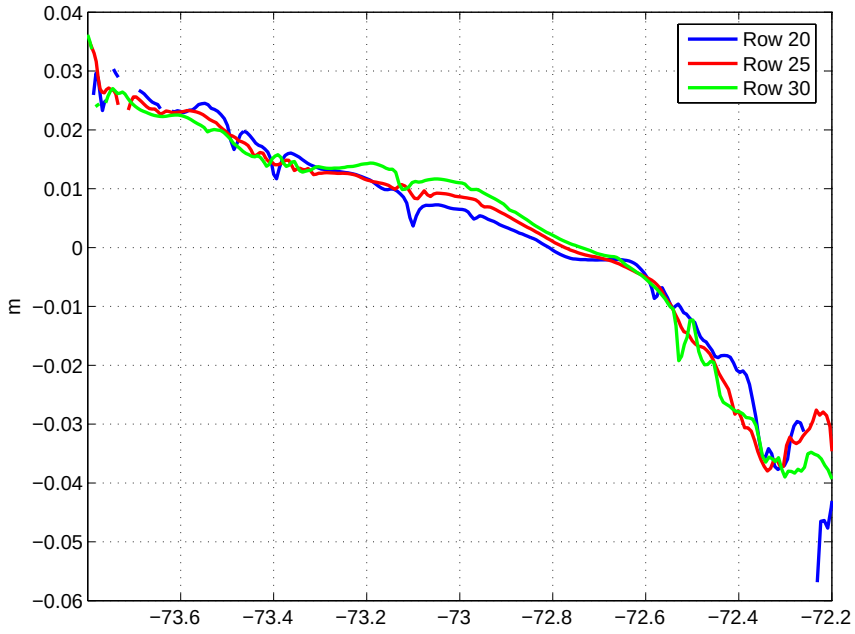

Figure 4.2. Longitudinal variation in mean sea level along the channel axis.

05/11/88 to 07/30/88. Without addressing details related to small scale topographic features, the near surface flow pattern (sigma level 9) is characterized by a concentrated seaward directed flow on the south side of the basin and a broad inflow on the north side of the basin. There is evidence for headland eddies in the central part of the basin. A distinctive feature of the mid-depth (sigma level 5) and lower level (sigma level 2) flow is an inflow concentrated over the deeper channel.

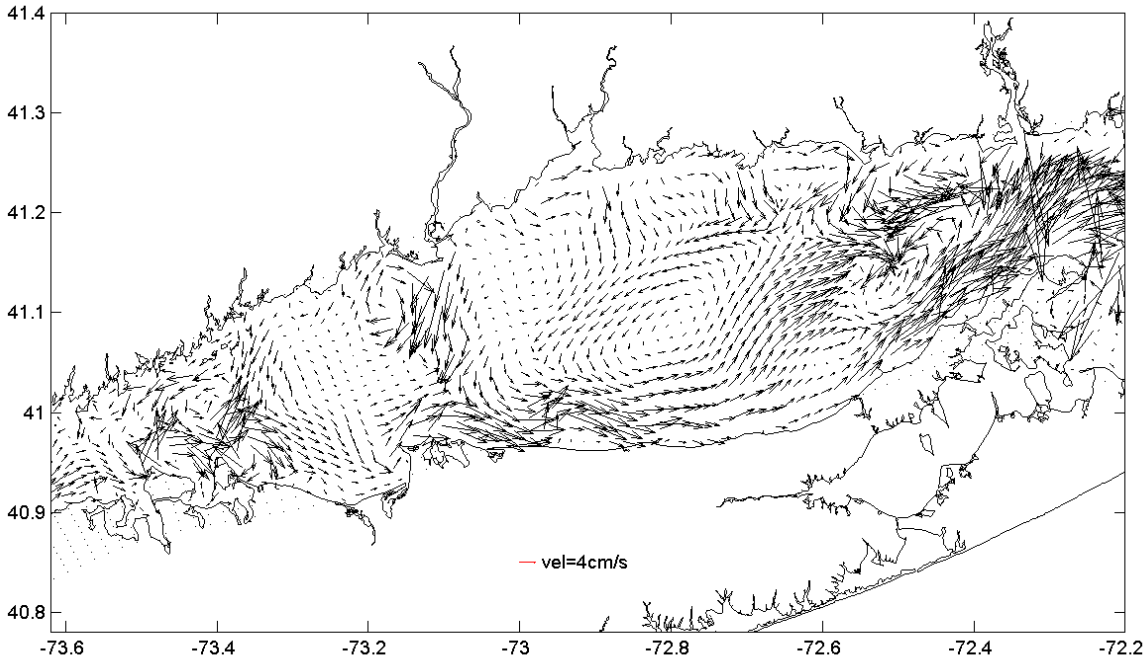

Figure 4.3. Residual Eulerian currents at sigma level 9.

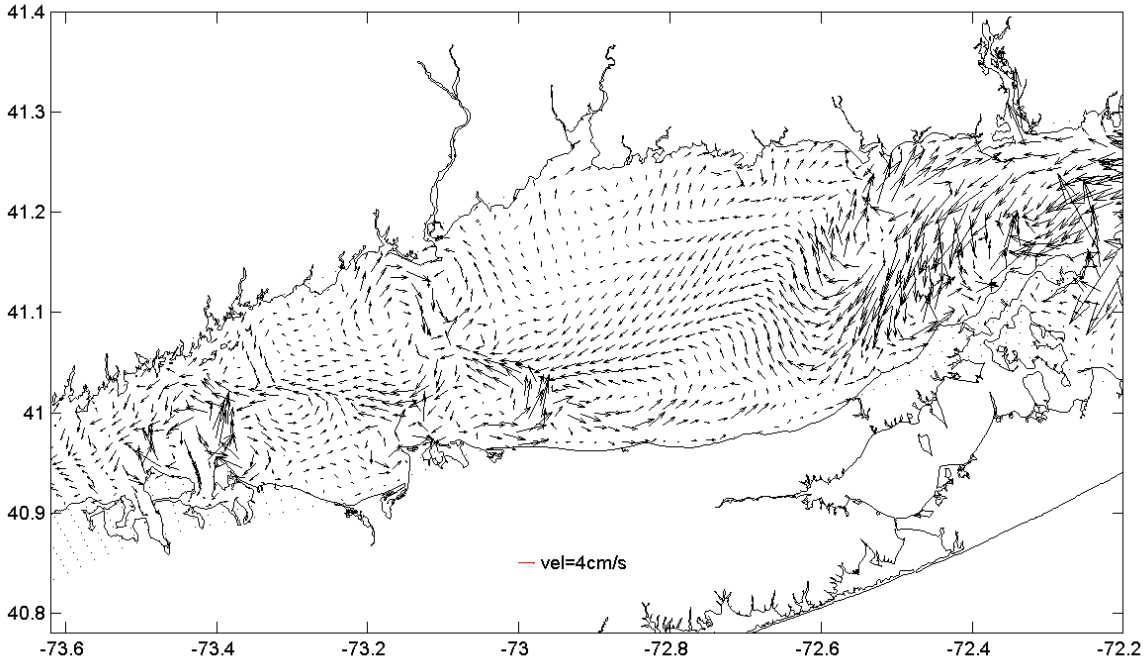

Figure 4.4. Residual Eulerian currents at sigma level 5.

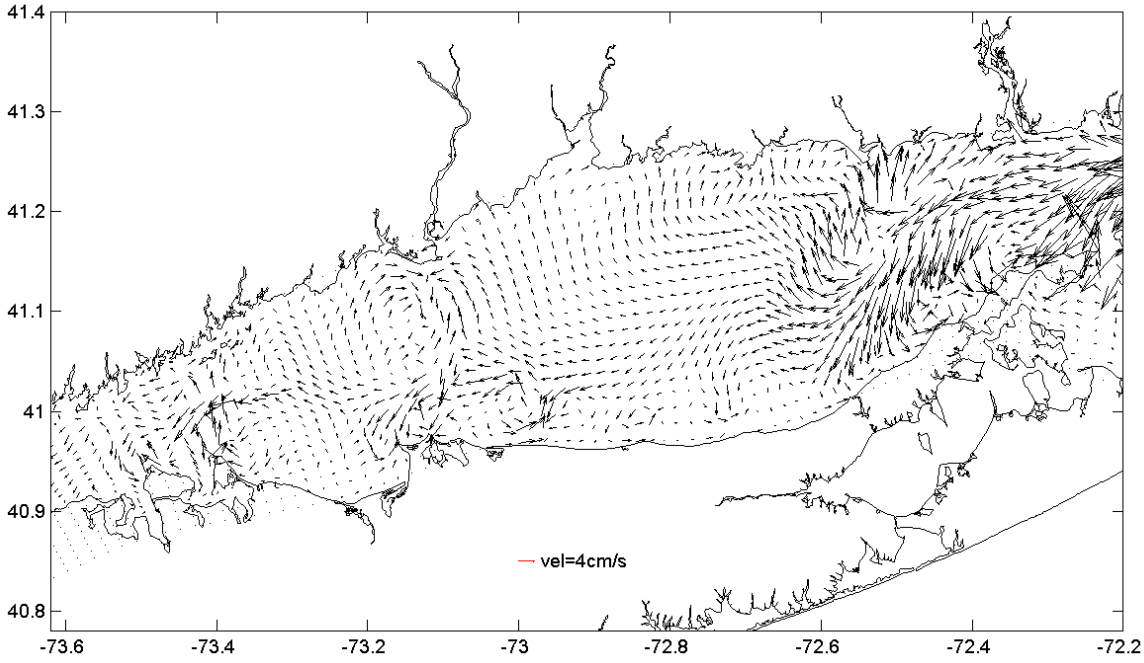

Figure 4.5. Residual Eulerian currents at sigma level 2.

4.3 Three-dimensional residual velocity and density

Fig. 4.6 shows residual velocity at the four lateral transects located in Fig. 3.4. Note that each section is presented for an observer looking towards the western end of the basin. There are a number of characteristic features in the velocity structure represented at each section. Sections show an inflow region concentrated over the channel and skewed towards the right side of the channel which penetrates nearly to the surface. Sections also show a concentrated surface intensified outflow over the southern side of the channel. Over the right side of the channel there is a weak surface intensified outflow. Residual lateral currents are spatially complex and do not show an easily defined coherent structure.

Lateral sections of mean density anomaly (Fig. 4.7) at the four transects provide insight into the degree of stratification and the lateral density structure controlling the lateral baroclinic pressure gradient. All sections show the intrusion of cold saline water in the main channel. They also provide evidence for boundary mixing which is most noticeable over the northern flank of the channel. There is also some evidence of an upward slope of the pycnocline towards the north side of the channel. The lateral baroclinic pressure gradient will be influenced by both the halocline slope and the bottom frontal structure associated with boundary mixing. This is discussed later in connection with the momentum balance at transect 144.

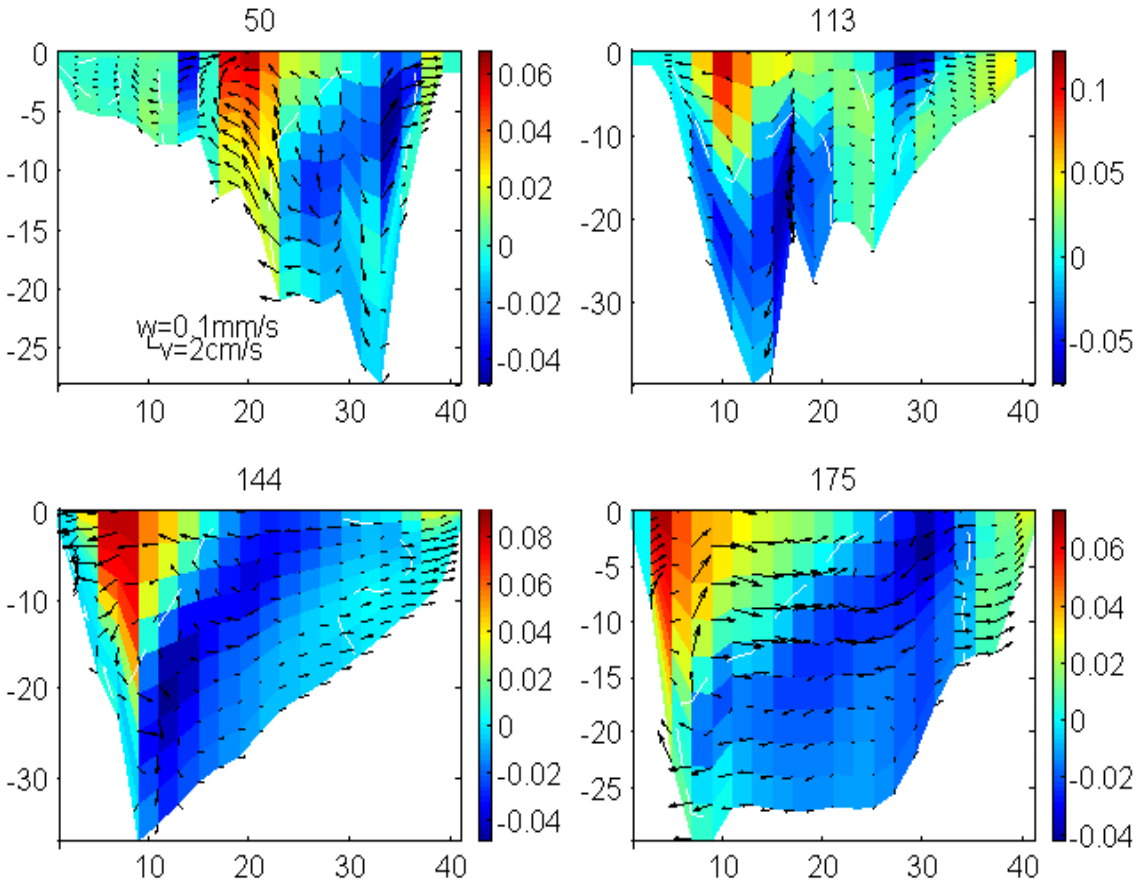

Figure 4.6. Lateral sections of residual longitudinal velocity (m/s) and residual lateral and vertical velocities at sections located in Fig. 3.4.

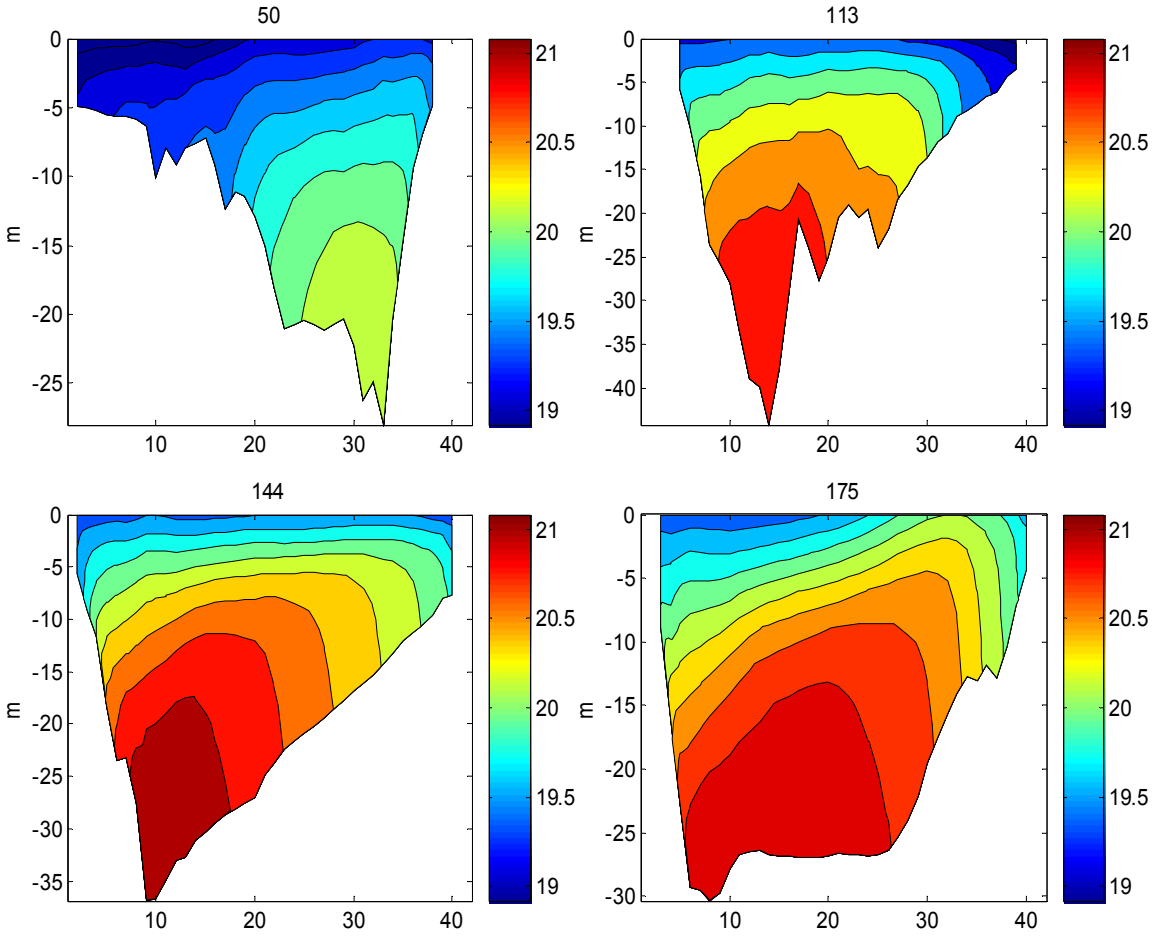

Figure 4.7. Lateral sections of mean density anomaly (kg/m^3) at sections located in Fig. 3.4.

4.4 Residual longitudinal and lateral momentum balances

As with our discussion of the tidal-period momentum balances in Section 3.3**,** we focus on a description of the residual momentum balances at transect 144 because of the simple topography. Primary objectives include a description of the structure of the advective accelerations driving the longitudinal residual flow, the effects on the structure of the residual longitudinal flow, and an assessment of the relative contributions of

advective and density forcing. As discussed earlier, it has been hypothesized by Ianiello (1981) and Wilson (1976) that advection and density forcing were comparable.

Fig. 4.8 shows the structure of terms in the residual longitudinal momentum equation obtained from model diagnostics averaged over the period 05/11/88 to 07/30/88. Tidal advection is seen to be a dominant forcing term, comparable to the baroclinic pressure gradient. Tidal advection ($<v\partial u/\partial y + w\partial u/\partial z>$) shows a distinctive structure; it is directed towards the west on the north side of the channel and towards the east on the south side of the channel. It changes sign abruptly as the bottom slope changes sign. There is a strong westward directed baroclinic pressure gradient within the channel. Within the upper water column the primary force balance is between pressure gradient and advection. Friction is important primarily within the lower water column.

Fig. 4.9 shows the structure of terms in the residual lateral momentum equation obtained from model diagnostics averaged over the same time period. Tidal advection is seen not to be a dominant forcing term. The baroclinic pressure gradient shows the influence of boundary mixing; it tends to be directed towards the north on the north side of the channel and towards the south on the south side of the channel. Fig. 4.6 shows that there is, in fact, northward directed near bottom flow on the north side of the channel at transect 144. The dominant lateral balance is seen to be geostrophic.

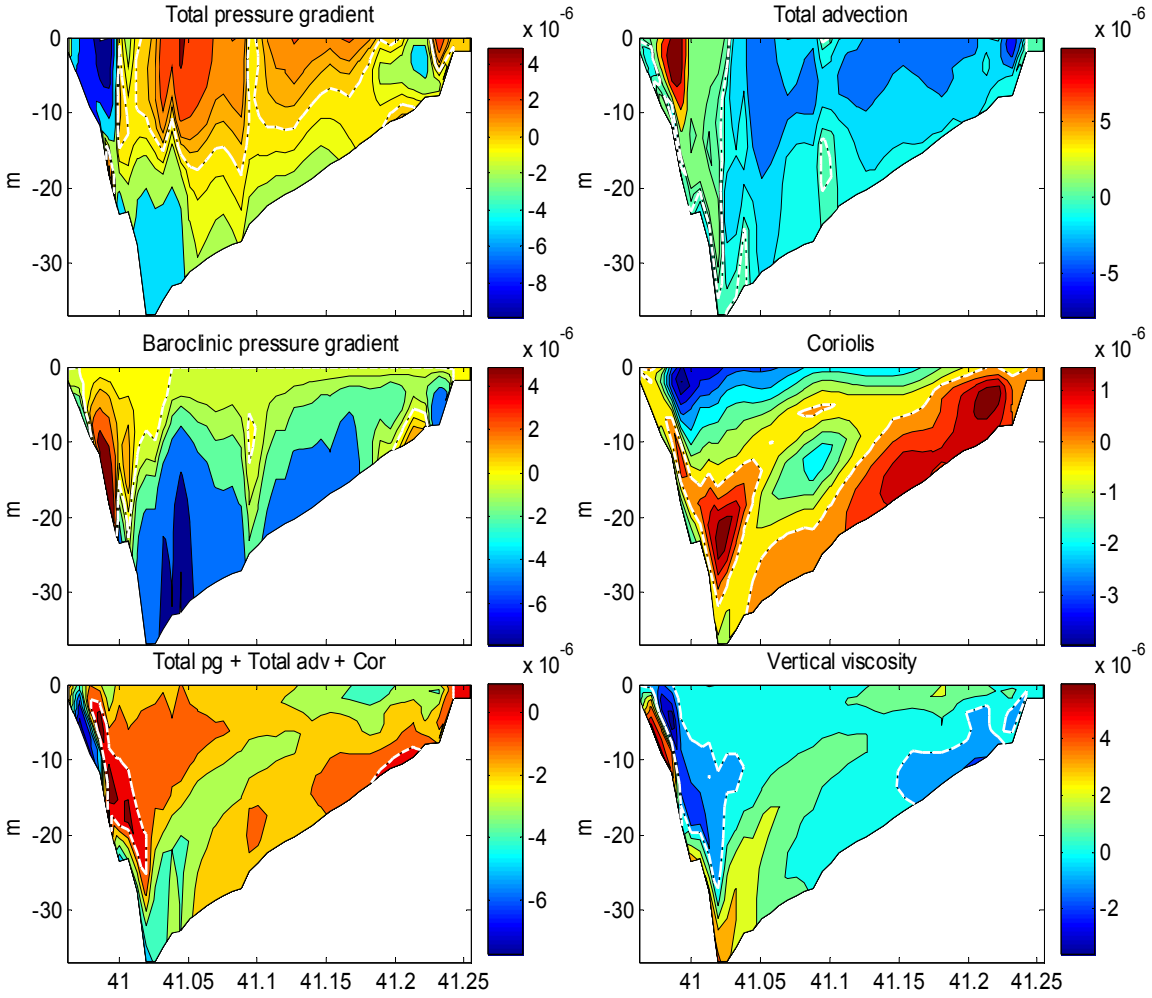

Figure 4.8. Lateral structure of terms in the residual longitudinal momentum equation at transect 144.

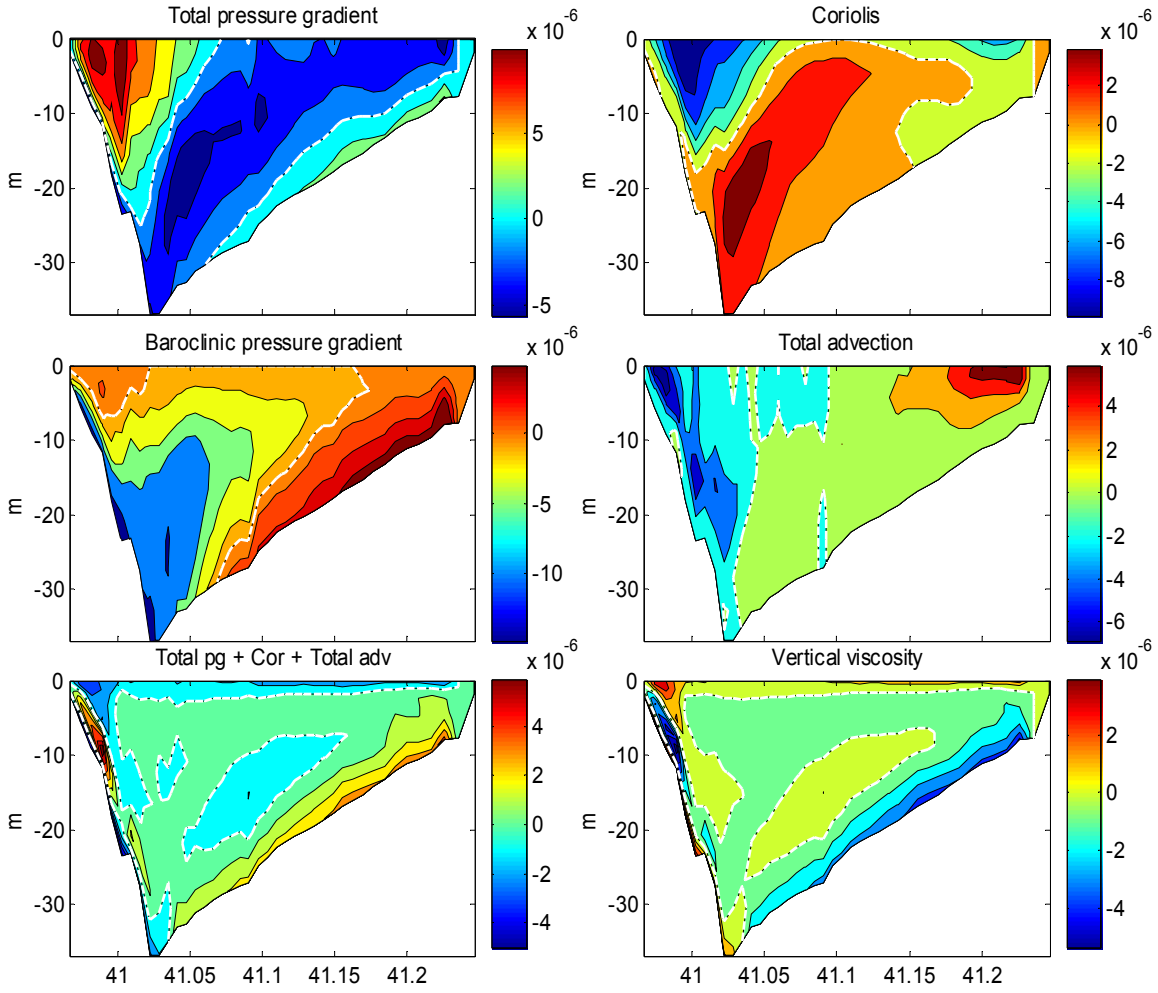

Figure 4.9. Lateral structure of terms in the residual lateral momentum equation at transect 144.

It is possible to obtain a somewhat more objective description of both the longitudinal and lateral residual momentum balance, including a description of how the momentum balance varies over the section by using Principal Component Analysis (PCA). PCA applied to the terms in the longitudinal momentum equation: Coriolis acceleration, total advection, total pressure gradient, and stress divergence in sequence, shows that first two modes account for 0.9 of the total spatial variance. The spatial structure of the first mode which accounts for 0.72 of the total variance is shown in

Fig.4.10; it is dominated by the structure of the advective terms. The eigenvector for this mode is [-0.05, 0.73, -0.69, -0.05], which provides a quantitative measure of the relative contribution of the four terms.

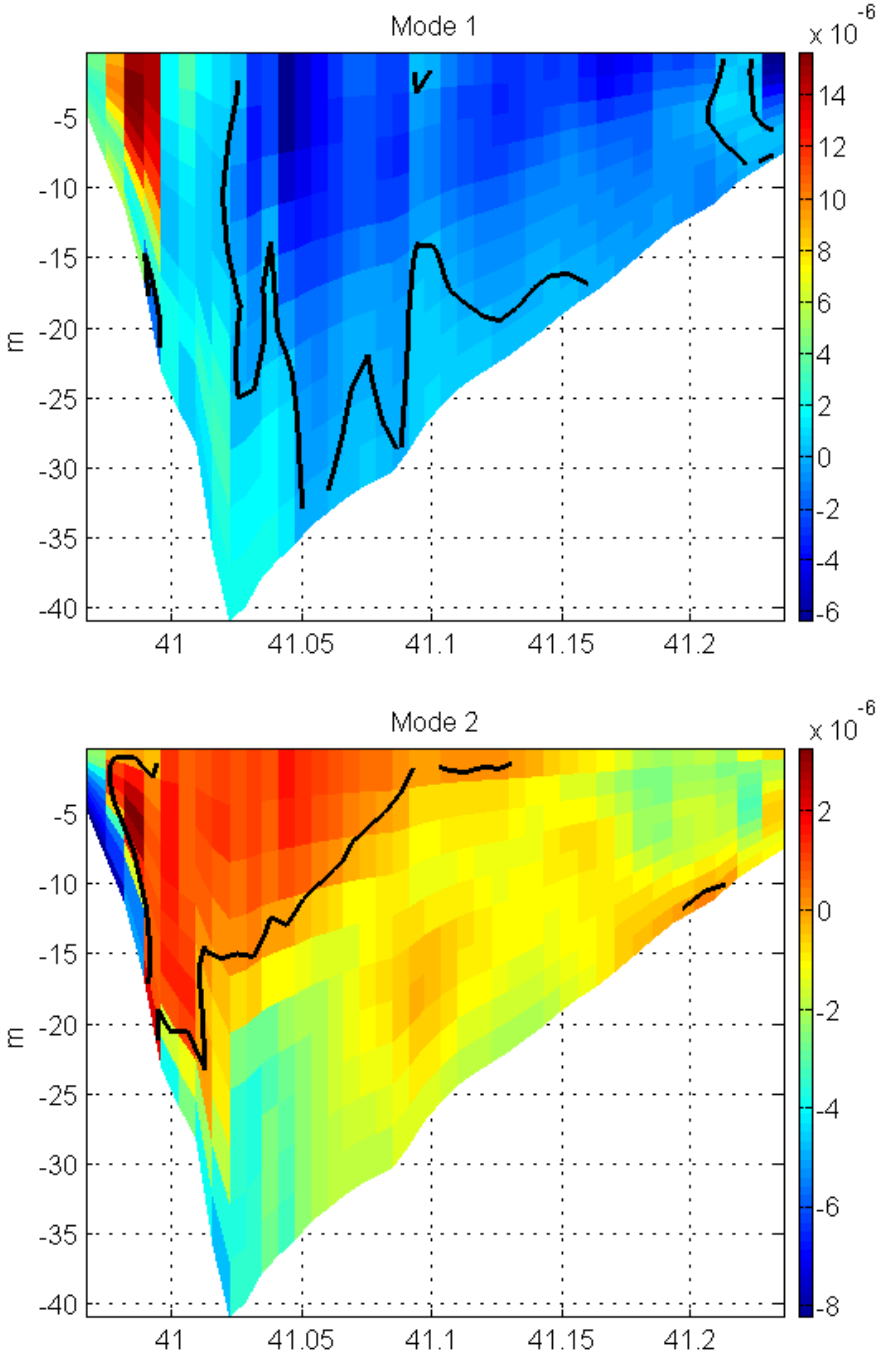

Figure 4.10. Mode 1 and mode 2 principal components (m/s^2) for the residual longitudinal momentum balance at transect 144.

The first mode balance is exclusively advection and pressure gradient. The spatial structure of the second mode which accounts for 0.18 of the total variance reflects the structure of the baroclinic pressure field. The eigenvector for this mode is [-0.28, 0.45, 0.55, -0.63].

PCA applied to the same terms in the lateral momentum equation shows that first two modes account for 0.93 of the total spatial variance. The spatial structure of the first mode which accounts for 0.75 of the total variance is shown in Fig. 4.11; it reflects a predominant geostrophic balance but there is some contribution from advection. The eigenvector for this mode is [0.51, 0.29, -0.81, -0.01]. The spatial structure of the second mode which accounts for 0.18 of the total variance reflects a Coriolis and advection balance. The eigenvector for this mode is [0.67, -0.71, 0.16, -0.12].

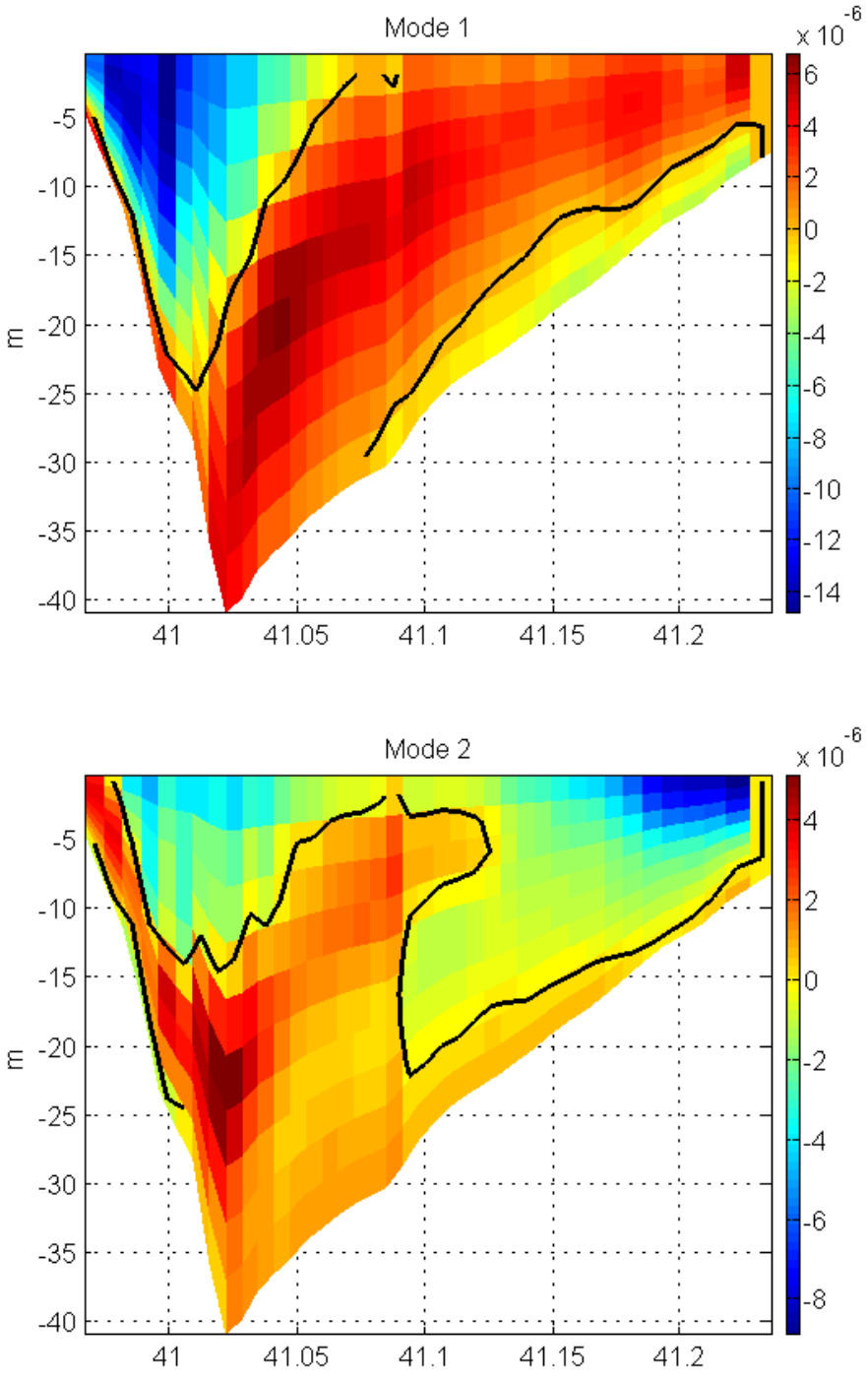

Figure 4.11. Mode 1 and mode 2 principal components (m/s^2) for the residual lateral momentum balance at transect 144.

4.5 Discussion

PCA applied to the residual longitudinal momentum balance provided a useful decomposition of the dominant momentum balances and their lateral structure. Mode 1 represented a balance between pressure gradient and advection. The barotropic model introduced by Winant (2008) for tidal residual motion in an elongated basin is based on the longitudinal and lateral momentum equation:

$$0 = f\alpha\bar{v} - \frac{1}{\kappa^2}\frac{\partial\overline{\eta}}{\partial x} + \frac{\delta^2}{2}\frac{\partial^2\bar{u}}{\partial z^2} - \overline{\left(u_0\frac{\partial u_0}{\partial x} + v_0\frac{\partial u_0}{\partial y} + w_0\frac{\partial u_0}{\partial z}\right)} \tag{4.1}$$

$$0 = -\frac{f}{\alpha}\bar{u} - \frac{1}{\alpha^2\kappa^2}\frac{\partial\overline{\eta}}{\partial y} + \frac{\delta^2}{2}\frac{\partial^2\bar{v}}{\partial z^2} - \overline{\left(u_0\frac{\partial v_0}{\partial x} + v_0\frac{\partial v_0}{\partial y} + w_0\frac{\partial v_0}{\partial z}\right)} \tag{4.2}$$

Where 'bar' denotes tidal average and u_0, v_0, w_0 are first order tidal velocities. For the parameter values introduced for LIS in Section 3.4, the second and fourth terms on the right side of the longitudinal equation (4.1) dominate, and so represent a balance between pressure gradient and advection, consistent with our first mode longitudinal balance. Similarly, the first and second terms on the right side of the lateral equation (4.2) dominate, consistent with our first mode lateral balance.

Further, the spatial structure of our advective terms (Figs. 4.8 and 4.10) is consistent with the structure found by Winant (2008) for similar parameter values, and by Huijts et al. (2008) for advection produced by Coriolis forcing. The primary longitudinal balance represented by Mode 2 is between pressure gradient and friction so it could be considered a density driven mode. We conclude that the structure of residual longitudinal flow at

transect 144 is then a superposition of that due to tidal advection and longitudinal density gradient with their distinctive patterns (Huijts et al., 2008).

Huijts et al. (2008) provided scaling from which the ratio of the advectively driven residual current to density driven residual current in an estuary can be estimated. This ratio is independent of vertical eddy viscosity and given by:

$$W = \frac{Q_t^2}{BAL^2} \Big/ \frac{H^3 g \partial\rho}{A\rho_0 \partial x} = \frac{Q_t^2 \rho_0 \Delta x}{BL^2 H^3 g \Delta\rho} = \frac{Q_t^2 \rho_0 \Delta x}{\alpha B^3 H^3 g \Delta\rho} \tag{4.3}$$

where A is the vertical eddy viscosity, Q_t is the semi-diurnal discharge, $\Delta\rho/\Delta x$ is the longitudinal density gradient, B is the basin width and H is the maximum depth. Estimating the parameters we obtain: $Q_t^2 = 1.6 \times 10^{11}$ m^6/s^2, $\rho_0 \Delta x / \Delta\rho = 2 \times 10^7$ m, and $B^3H^3g = 1.0 \times 10^{19}$ m^7/s^2. This gives then for W

$$W = \frac{Q_t^2 \rho_0 \Delta x}{\alpha B^3 H^3 g \Delta\rho} = (3.2 \times 10^{18} m^7/s^2)/(\alpha \times 1.0 \times 10^{19} m^7/s^2) \approx 1 \; for \; \alpha \approx 0.3$$

So we expect advectively driven and density driven currents to be of the same order in LIS.

Chapter 5

Observations and Synthesis

5.1 Observations

Current observations have been collected in LIS since the spring of 2003 using ADCPs mounted on passenger ferries traversing the central and eastern basins (http://www.sunysb.edu/soundscience). Fig. 5.1 shows cruise tracks for the P.T. Barnum in central LIS connecting Port Jefferson, NY and Bridgeport, CT, indicating operational shifts in vessel path. Fig. 5.1 also shows the approximate track of the MV John H. in eastern LIS connecting Orient Pt., NY and New London, CT. The central LIS ferry track coincides with model transect 113. While not making objective comparisons between observed and simulated currents, we are able to compare features in the lateral structure of both tidal and residual longitudinal currents at this transect. We are also able to compare observed and simulated exchange fluxes at both ferry transects.

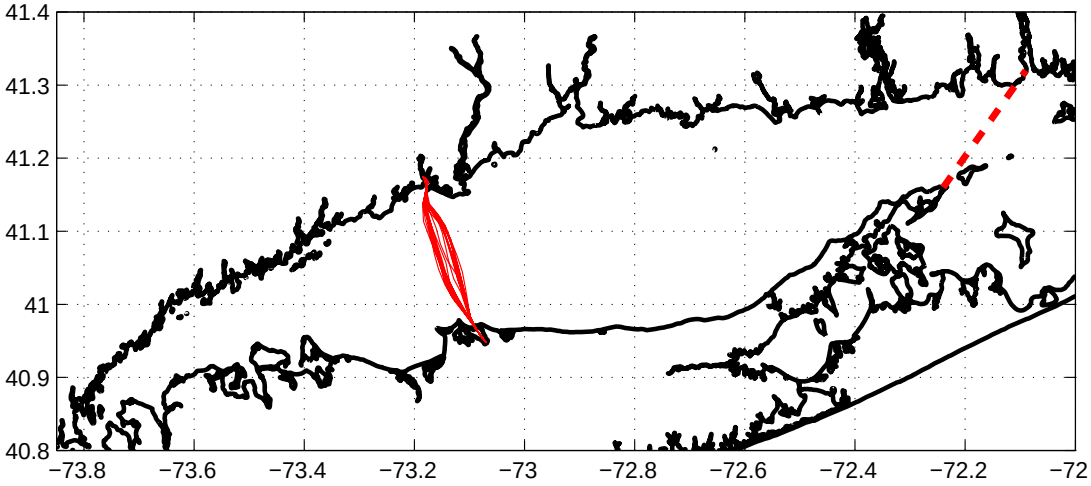

Figure 5.1. Cruise tracks of P.T. Barnum in central LIS (solid red lines) and approximate track of MV John H. in eastern LIS (dashed red line).

The central LIS ADCP is a 600 kHz Work Horse manufactured by RD Instruments. The vertical bin size is set to 2m and the center of the first good bin is at 5m. Data from bins deeper than approximately 0.90 of the water column between the transducer and the bottom are discarded because of side lobe contamination. The vessel traverses central LIS approximately eleven times per day.

The data we used for this study were collected from 07/19/03 to 08/13/03. The individual ping data were recorded and the calibration and quality control based on percent good was then applied to the raw data. Measured vector velocities were decomposed into orthogonal along-estuary and across-estuary components, aligned with the x and y direction on transect 113 in the numerical model.

a. Current structure

Figs. 5.2 and 5.3 provide a comparison of residual current structure obtained from ADCP observations (07/19/03 to 08/13/03) and model simulations at transect 113 (05/11/88 to 07/30/88). In making this comparison it is important to remember that the first good ADCP bin is centered on 5m. There is similarity in both the vertical and lateral structure, and the comparison is encouraging.

Figs. 5.4 and 5.5 provide a comparison of the lateral structure of M_2 longitudinal current amplitude obtained from ADCP observations and model simulations at transect 113 for the time periods described above. The comparisons show very good agreement in vertical and lateral M_2 amplitude structure. The companion M_2 phase diagrams are shown in Figs. 5.6 and 5.7. Feature associated with the near bottom phase advance as well as the phase advance on channel flanks compares favorably.

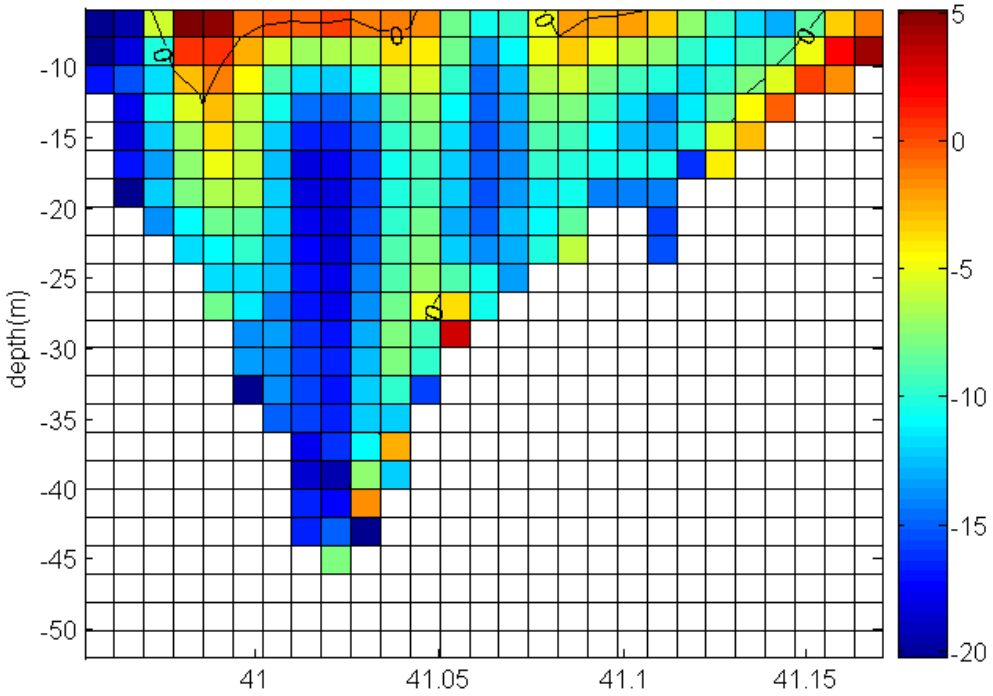

Figure 5.2. Residual velocity (cm/s) from ADCP observations (07/19/03 to 08/13/03).

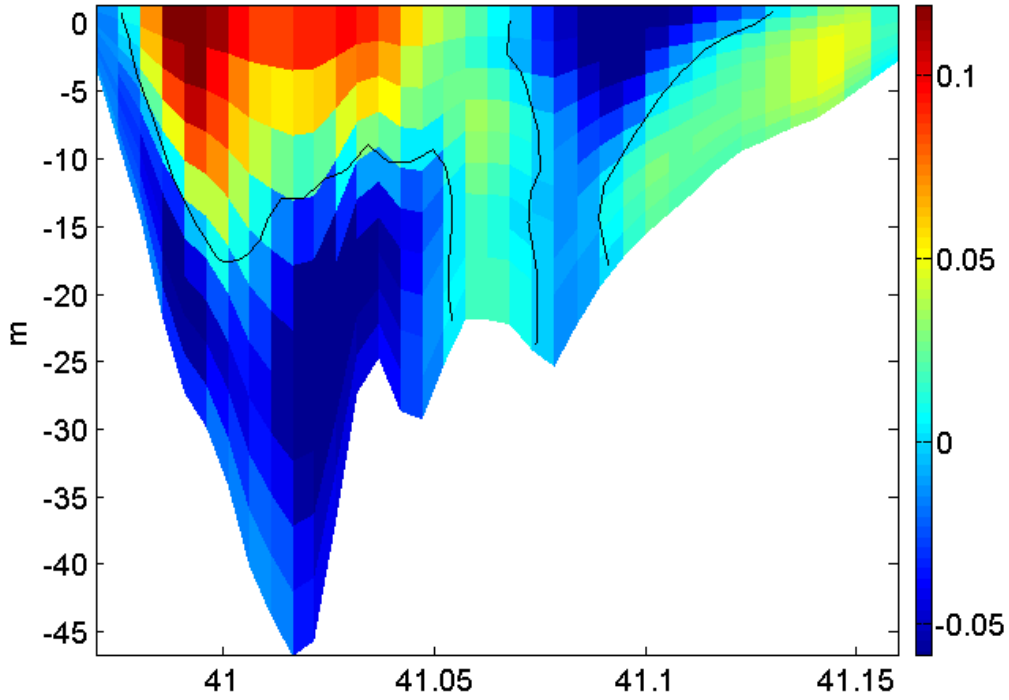

Figure 5.3. Residual velocity (m/s) at model transect 113 (05/11/03 to 07/30/03).

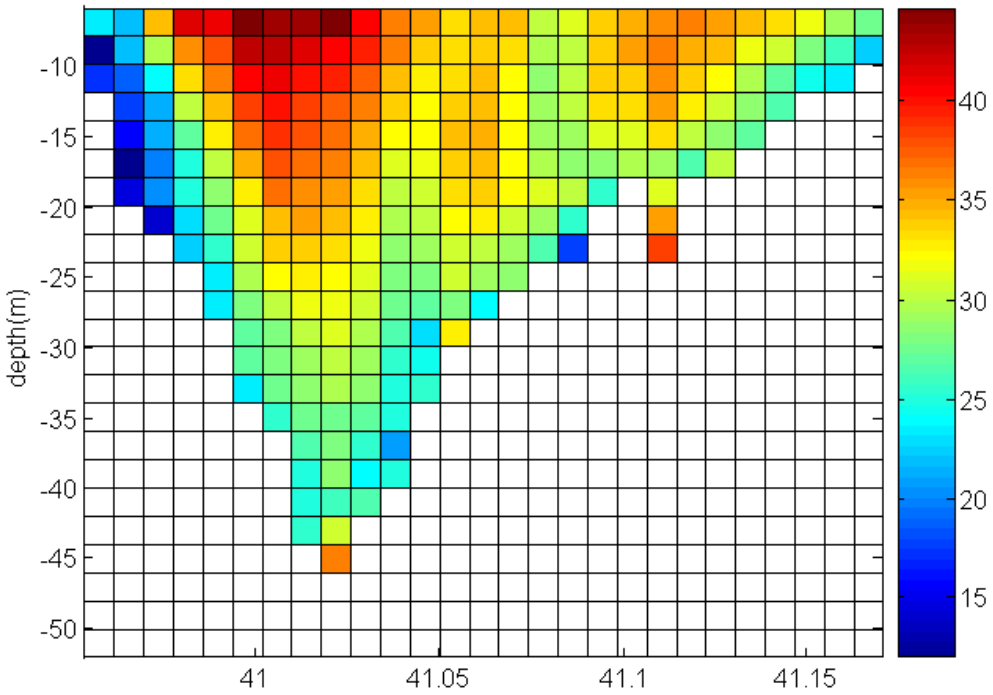

Figure 5.4. M_2 amplitude (cm/s) from ADCP observations (07/19/03 to 08/13/03).

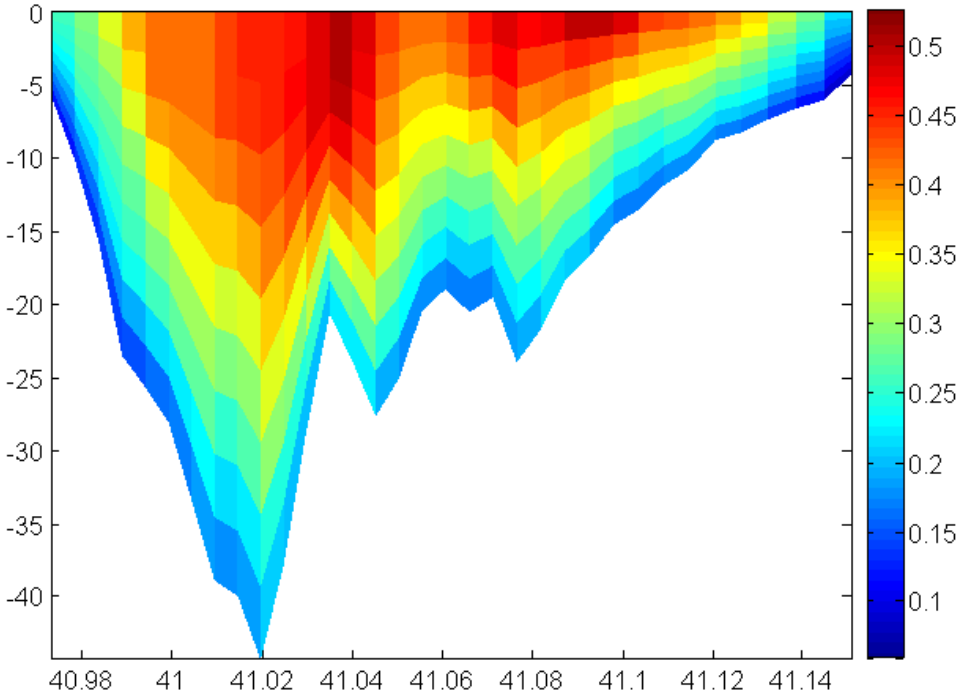

Figure 5.5. M_2 amplitude (m/s) at model transect 113 (05/11/03 to 07/30/03).

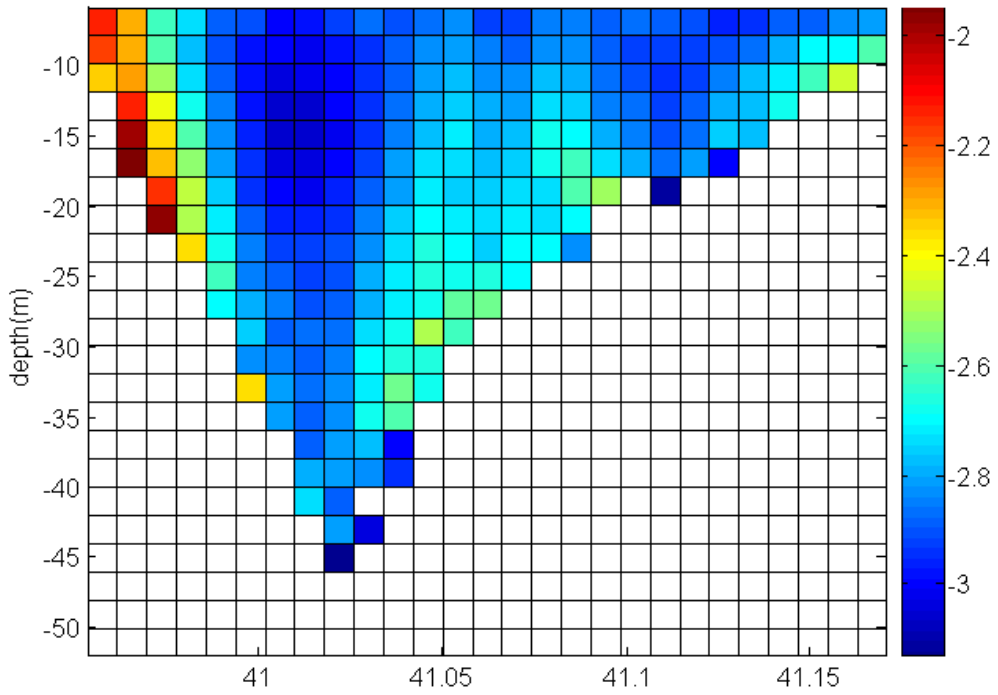

Figure 5.6. M_2 phase (radians) from ADCP observations (07/19/03 to 08/13/03).

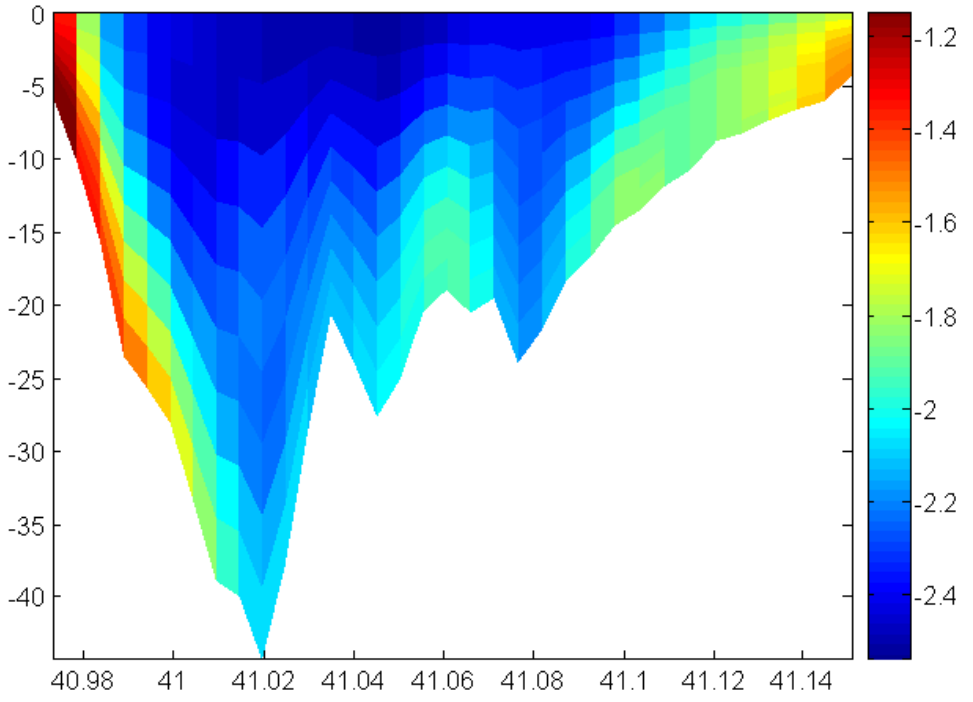

Figure 5.7. M_2 phase (radians) at model transect 113 (05/11/03 to 07/30/03).

b. Exchange transports

The exchange volume transport through the ADCP ferry section was calculated as the sum of all the product of the westward directed residual velocity and the fixed area of each cell. Exchange transport calculated in this way does reflect any possible contribution from Stokes transport. Table 5.1 shows the exchange transport estimated for four different time periods. The mean volume transport is approximately -1.1×10^4 m^3/s, where the minus sign associated with table entries indicates transport towards the west into the basin. The transports in Table 5.1 were calculated from residual velocities obtained from least squares analyses; the two columns show results for M_2 least squares analysis, and for M_2,N_2,S_2 least squares analysis.

		Transport (m^3/s)	
	PERIODS	M_2 component only	M_2, N_2, S_2
	05/19/2004 to 07/19/2004	-1.2090×10^4	-1.1837×10^4
	07/15/2004 to 08/21/2004	-1.0443×10^4	-1.0934×10^4
	08/06/2004 to 09/28/2004	-1.0108×10^4	-9.3648×10^3
	09/12/2004 to 11/08/2004	-1.2326×10^4	-1.0215×10^4

Table 5.1. Exchange transport through the ADCP transect for four different time periods.

Crowley (2005) calculated residual exchange transports through six lateral transects in LIS over the duration of her simulations from April to September, 1988. The transports and the standard deviations from her calculation are shown in Fig. 5.8. Note that transect 113 is located approximately at longitude -73.12^o W, and that the westward volume transport through this section is about -1.05×10^4 m^3/s, which is in remarkable agreement with the mean transport from Table 5.1. Similarly, Crowley (2005) estimated exchange

transports through her easternmost transect approaching -2×10^4 m^3/s. This transport is consistent with the estimate of –2.2×10^4 m^3/s obtained by Codiga and Aurin [2007] for the eastern LIS ferry transect.

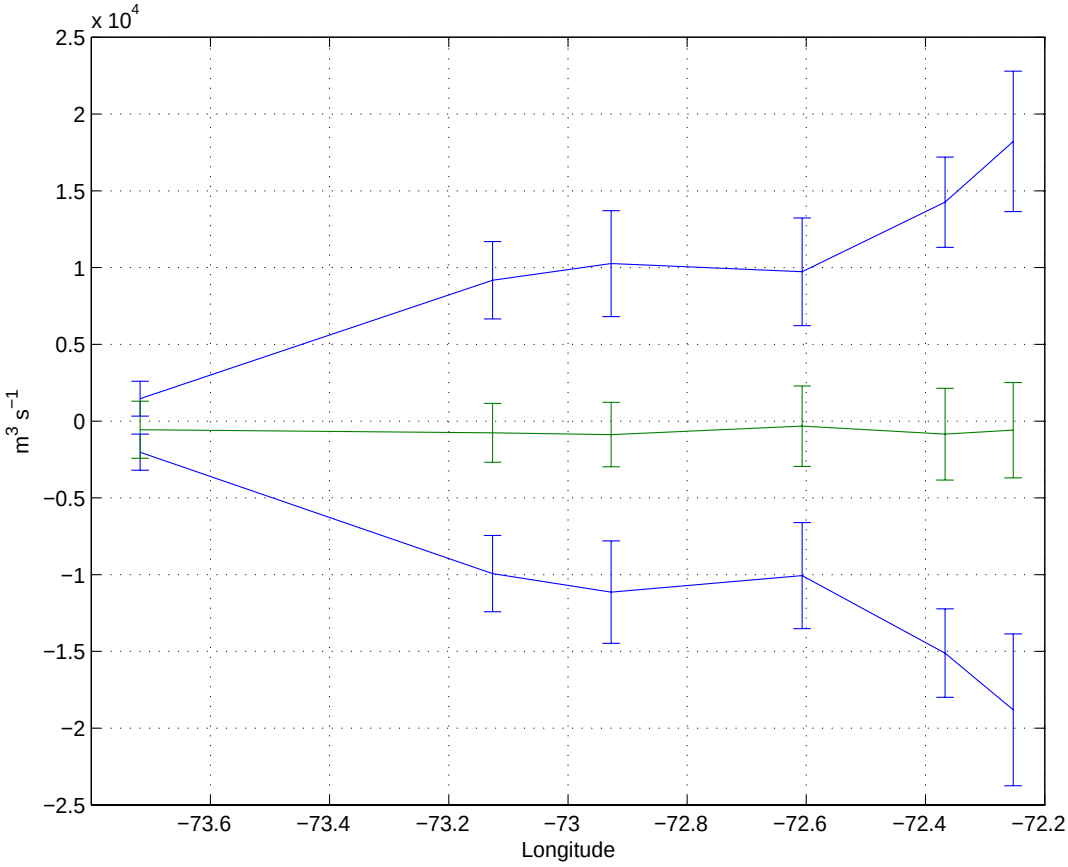

Figure 5.8. Means and standard deviations of exchanged (blue) and net (green) volume transport in Long Island Sound. (Crowley, 2005)

5.2 Synthesis

PCA applied to the longitudinal residual momentum balance highlighted the important contributions of both advection and baroclinic pressure gradient in driving the residual longitudinal motion. For a section within the central basin, the first mode represents a predominant balance between advection and pressure gradient. The lateral

structure of this mode reflects the structure of the advective acceleration. The second mode represents a predominant balance between pressure gradient and stress divergence, and the lateral structure of this mode reflects the structure of the baroclinic pressure gradient. For the lateral momentum balance the first mode represents a predominant geostrophic balance and the lateral structure reflects the structure of the Coriolis acceleration.

Additional insight into the basic question of the relative contributions of advection and baroclinicity in driving residual motion is obtained by diagnosing the barotropic pressure gradient associated with the residual elevation field shown in Fig. 4.1. If we accept that the lateral barotropic pressure gradient essentially balances the Coriolis acceleration associated with the surface longitudinal current, then it remains to partition the longitudinal barotropic gradient into contributions which balance the depth averaged advection, baroclinic pressure gradient, Coriolis acceleration, and stress divergence:

$$0 = f\bar{v}^* - g\frac{\partial \bar{\eta}^*}{\partial x^*} - \frac{gz^*}{\rho_0}\frac{\partial \rho}{\partial x^*} + \frac{\partial \bar{\tau}^*}{\partial z^*} - \overline{\left(u_0^* \frac{\partial u_0^*}{\partial x^*} + v_0^* \frac{\partial u_0^*}{\partial y^*} + w_0^* \frac{\partial u_0^*}{\partial z^*} \right)} \qquad (5.1)$$

where (*) denotes a dimensional variable to be distinguished from non-dimensional variables in equations 4.1 and 4.2. Figs. 5.9-5.12 show the depth-averaged terms in equation 5.1 as a function of lateral position for sections 50, 113, 144 and 175. They emphasize that advection represents driving force comparable to baroclinicity at all four sections. Fig. 5.9 indicates that advection is an important driving force even in the western basin.

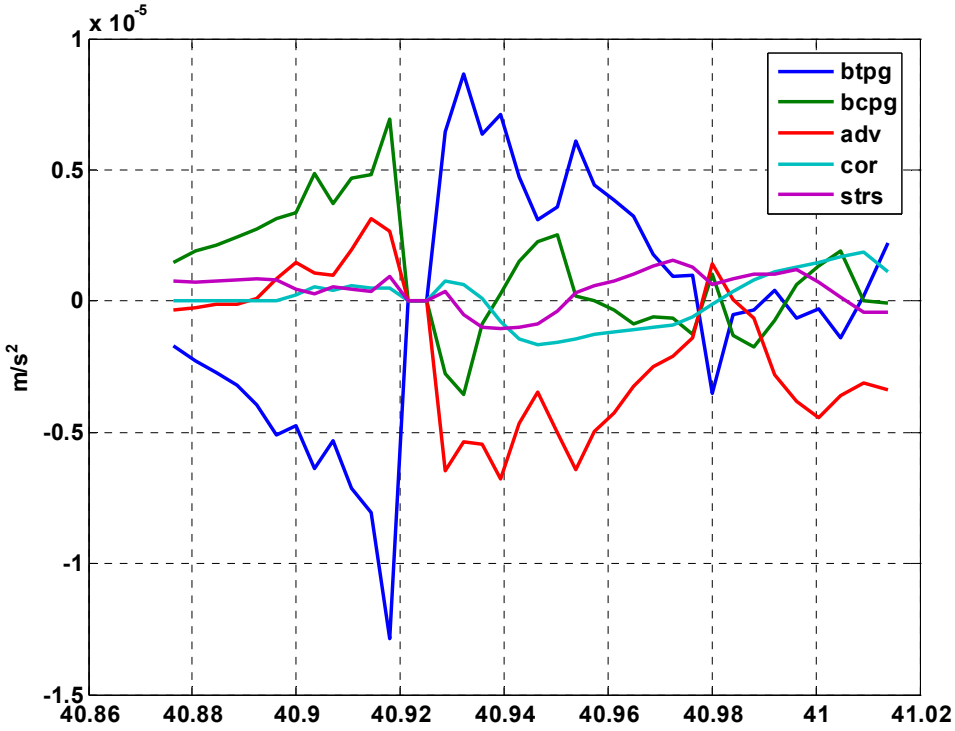

Figure 5.9 Depth averaged residual longitudinal momentum terms at transect 50.

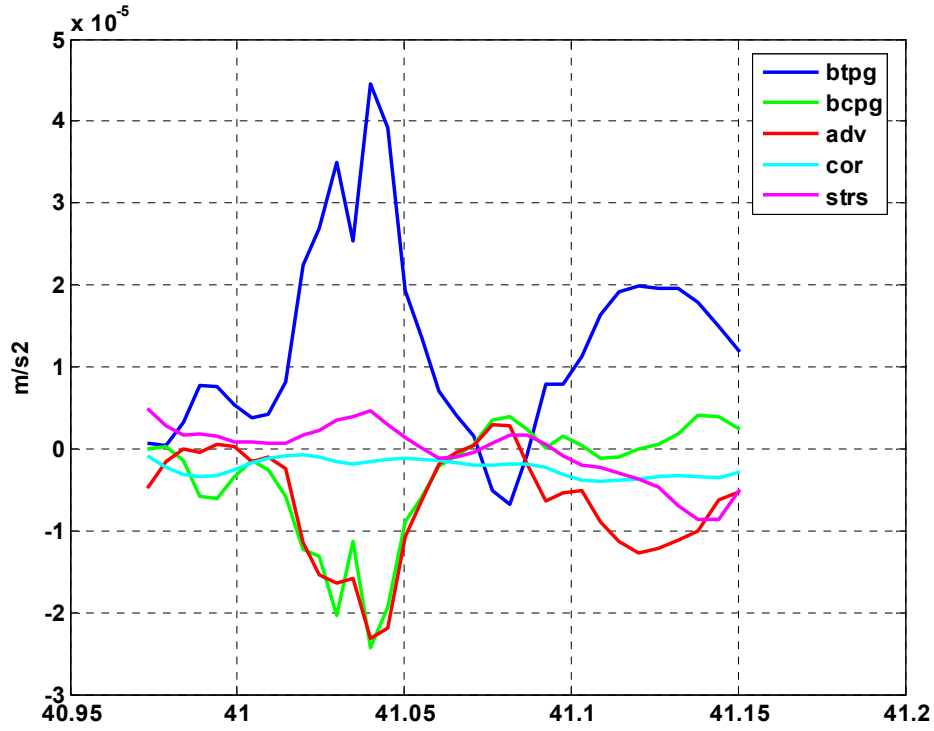

Figure 5.10 Depth averaged residual longitudinal momentum terms at transect 113.

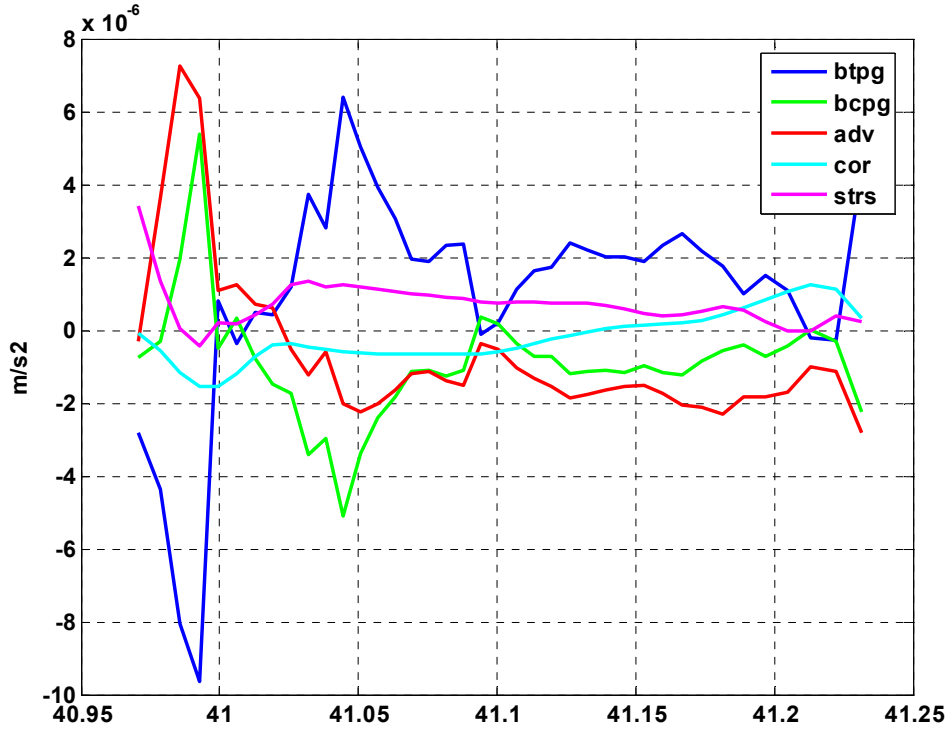

Figure 5.11 Depth averaged residual longitudinal momentum terms at transect 144.

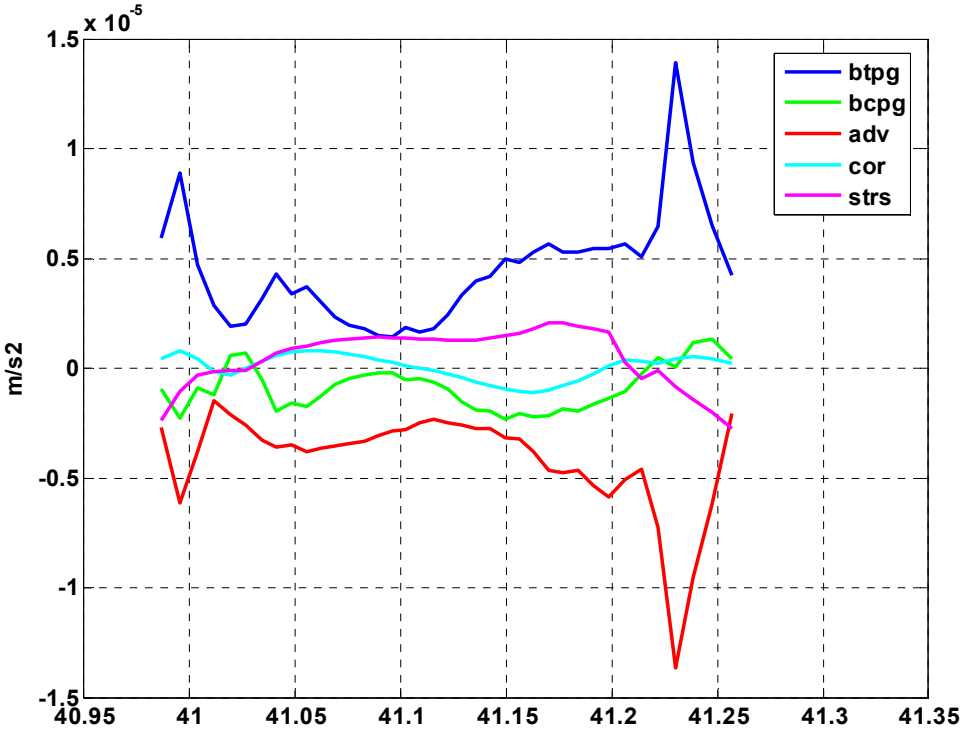

Figure 5.12 Depth averaged residual longitudinal momentum terms at transect 175.

5.3 Conclusions

The barotropic scaling proposed by Winant (2007) is consistent with tidal period longitudinal and lateral momentum balances in LIS. Longitudinal balance is primarily pressure gradient and acceleration with contribution from stress divergence at depth. Lateral balance is primarily pressure gradient, Coriolis and acceleration. Tidal period lateral motion is produced primarily by Coriolis forcing rather than differential advection or boundary mixing, and this Coriolis forced lateral motion will contribute to the maintenance of the residual motion in the basin.

Barotropic scaling proposed by Winant (2008) is consistent with residual longitudinal and lateral momentum balances in LIS. The dominant longitudinal balance is between advection and pressure gradient, and the dominant lateral balance is geostrophic. Coriolis forcing of tidal period lateral motion contributes to residual advection primarily through lateral advection of longitudinal momentum. Advectively driven and density driven residual longitudinal currents are of the same order in LIS, consistent with the scaling of Huijts at al. (2008). A coherent picture of residual lateral currents in LIS is difficult to obtain.

Available ADCP observations show extremely good agreement with model simulations as far as westward directed exchange flux. They also show good agreement with lateral structure of residual longitudinal currents, and the lateral structure of the amplitude and phase of M_2 constituent.

Interesting future studies could relate to reconciling our numerical results with analytical results obtained by Li and O'donnell (1997, 2005).

References:

Bogden, P. S. and J. O'Donnell, 1998: Generalized inverse analysis of current measurements from a moving ship: estimating the tidal and non-tidal flows in Long Island Sound. J. Marine Res., 56, 995-1027.

Chant, R. J. and R. E. Wilson, 1997: Secondary circulation in a highly stratified estuary. J. Geophys. Res., 102, 23207-23216.

Chant, R. J. (2002), Secondary circulation in a region of flow curvature: Relationship with tidal forcing and river discharge, *J. Geophys. Res.*, 107(C9), 3131, doi:10.1029/2001JC001082.

Chen, S-N and L. P. Sanford, 2008: Lateral circulation driven by boundary mixing and the associated transport of sediments in idealized partially mixed estuaries. Continental Shelf Research, *In Press.*

Cheng, P., 2007: Modeling sediment transport in the estuarine environment: effects of tidal asymmetry, lateral circulation and sediment-induced stratification. PhD Dissertation, Marine Sciences Research Center, Stony Brook University, Stony Brook, NY, 154 pp.

Cheng, P., R. E. Wilson, R. J. Chant and R. D. Flood, 2008: A numerical study of lateral circulation in a partially mixed estuary. Journal of Geophy. Res., *Under Revision.*

Codiga, D. L. and D. A. Aurin, 2007: Residual circulation in eastern Long Island Sound: Observed transverse-vertical structure and exchange transport. Continental Shelf Research, 27(1), 103-116.

Crowley, H. A., 2005: The seasonal evolution of thermohaline circulation in Long Island Sound. PhD Dissertation, Marine Science Research Center, Stony Brook University 114pp.

Geyer, W. R., J. H. Trowbridge, and M. M. Bowen, 2000: The dynamics of a partially mixed estuary. J. Phys. Oceanogr., 30, 2035-2048.

Geyer, W.R., R. Chant and R. Houghton, 2008: Tidal and spring-neap variations in horizontal dispersion in a partially mixed estuary. Journal of Geophy. Res., *In Press.*

Huijts, K.M.H., H.M. Schuttelaars, H.E. de Swart and C.T. Friedrichs, 2008: Analytical study of the transverse distribution of along-channel and transverse residual flows in tidal estuaries. Continental Shelf Research, *In Press.*

Kasai, A., A. E. Hill, T. Fujiwara, and J. H. Simpson, 2000: Effect of the Earth's rotation on the circulation in regions of freshwater influence. J. Geophys. Res., 105 (C7), 16961–16969.

Ianniello, J. P., 1981: Tidally-induced residual currents in Long Island and Block Island Sounds. Estuarine, Coastal and Shelf Science, 12,177-191.

Lacy, J. and S. G. Monismith, 2001: Secondary currents in a curved, stratified channel, J. Geophys. Res (Oceans) 106(C12), 31,283-31,302

Lerczak, J. A., and W. R. Geyer, 2004: Modeling the lateral circulation in straight, stratified Estuaries. J. Phys. Oceanogr., 34, 1410-1428.

Li, C., and J. O'Donnell, 1997: Tidally driven residual circulation in shallow estuaries with lateral depth variation. J. Geophys. Res*., 102*(C13), 27,915–27,929.

Li, C. and J. O'Donnell, 2005: The effect of channel length on the residual circulation in tidally dominated channels. J. Phys. Oceanogr., 35, 1826-1840.

Officer, C. B. 1976. Physical Oceanography of Estuaries (and Associated Coastal Waters). John Wiley, NY, 465 pp.

Shchepetkin, A. F. and J. C. McWilliams, 2005: Regional Ocean Model System: a split-explicit ocean model with a free-surface and topography-following vertical coordinate. Ocean Modelling, 9, 347–404.

Valle-Levinson, A. and R. E. Wilson, 1998: Effects of rotation and mixing on volume exchange in Eastern Long Island Sound. Estuarine, Coastal and Shelf Science, 46, 573-585.

Valle-Levinson, A., K. C. Wong, and K. M. M. Lwiza, 2000: Fortnightly variability in the transverse dynamics of a coastal plain estuary. J. Geophys. Res., 105 (C2), 3413–3424.

Vieira, M. E. C. 2000: The long-term residual circulation in Long Island Sound. Estuaries 23, 199-207.

Wilson, R. E. 1976: Gravitational circulation in Long Island Sound. Estuarine and Coastal Marine Science 4, 443-453.

Winant, C. D., 2007: Three-dimensional tidal flow in an elongated, rotating basin, Journal of Physical Oceanography, 37, 2345-2362.

Winant, C. D., 2008: Three-dimensional residual tidal circulation in an elongated, rotating, basin, J. Phys. Oceanogr., *In Press*.